Gondwana Research xxx (xxxx) 1–25

Contents lists available at ScienceDirect

Gondwana Research

journal homepage: www.elsevier.com/locate/gr

Effects of multi-extensional tectonics in a cratonic area: 3D numerical modeling and implications for the Congo basin

Francesca Maddaloni [a], Magdala Tesauro [a, b, *], Taras V. Gerya [c], Alberto Pastorutti [a], Carla Braitenberg [a], Damien Delvaux [d], Jessica Munch [c]

[a] Department of Mathematics and Geosciences, University of Trieste, Trieste, Italy
[b] University of Utrecht, Department of Geosciences, the Netherlands
[c] Institute of Geophysics, ETH Zürich, Zurich, Switzerland
[d] Royal Museum of Central Africa, Tervuren (BRX), Belgium

ARTICLE INFO

Article history:
Received 11 March 2022
Received in revised form 31 July 2022
Accepted 2 September 2022

Handling Editor: S. Kwon

Keywords:
Intracratonic basins
Congo basin
Multi-divergent velocity
3D numerical models
Forward gravity models

ABSTRACT

Different hypotheses have attempted to explain the long-lasting subsidence of the intracratonic basins, characterized by prolonged intervals of low rate subsidence, alternating with episodic accelerations in subsidence rates. Among them, the Congo Basin (*CB*) occupies a large part of the Congo Craton, derived from the amalgamation of different cratons. Previous studies demonstrated that the *CB* formed from a rift phase, during the late Mesoproterozoic. This extensional phase could have been the effect of the action of a slow multi-directional extension on a cratonic lithosphere, which has induced the initial subsidence of the *CB*. We investigated this tectonic scenario with 3D numerical thermomechanical models, using bi-directional N—S/E-W intra-cratonic extension with uniform velocity applied for up to 200 Myr. We assumed that the amalgamation of several cratonic blocks left a rectangular region with warm and more fertile lithosphere in the model centre, having a size of 10 % or 20 % of the total model area. Numerical results show the formation of an almost circular subsided area in the central part of the model, due to the crustal and lithospheric thinning above the asthenosphere upwelling. We also observe series of topographic highs and lows inside the subsided area and significant uplift at the transition zones towards the almost undeformed cratonic parts. At a later stage (>100 Myr), the topographic depression becomes intersected by two nearly orthogonal, elongated rift structures (quadruple junction), which tend to raise their surface topography. These features well represent the first order heterogeneity characterizing the *CB* basement, considering that its depth has been further modified by tectonic and climatic events. The formed structures are input for static and dynamic forward gravity models and the outputs compared with the present-day gravity field. In this way, the consistency between the modelled and observed main structures of the *CB* is demonstrated.

1. Introduction

The most suitable areas to study the long-term evolution of the continental interiors are the parts of cratons overlaid by a long record of sedimentary deposition. These contain the memory of the processes that are responsible for the past deformations and are readily available in intracratonic basins (*ICBs*). Different hypotheses (e.g., lithospheric stretching and subsequent thermal contraction, crustal and mantle phase changes, changes in the intraplate stress field, convective instabilities in the mantle, inherited heterogeneities) attempted to explain the long-lasting subsidence of these basins, characterized by prolonged intervals of low rate subsidence, alternating with episodic accelerations in subsidence rates (e.g., Klein and Hsui, 1987, Burke and Gunnel, 2008, Downey and Gurnis, 2009, Crosby et al., 2010, Buiter et al., 2012, Armitage and Allen, 2012; Perron et al., 2020). However, several *ICBs* originated from one or more rift phases, such as the Parnaiba basin (de Wit and Linol, 2015) and the basins of north-central Africa (e.g., Burke and Gunnel, 2008). This is not surprising, considering that the heating of a convecting mantle, accumulated at the base of a semi-stationary thick plate, can induce tensional stress, leading to asthenospheric mantle updoming and consequent basin formation (e.g., Gurnis, 1988; Phillips and Bunge 2007). In some of the *ICBs*, the rift phase occurred during the continental break-up. A number of long-lived *ICBs* in North America, such as the Michigan, Illinois, and Williston basins, developed as distinct circular or oval depocentres at about 520 Myr (e.g., Klein and Hsui, 1987), associated with the break-up of South America-Laurentia from Gondwanan superassembly. In Australia, a large *ICB*,

* Corresponding author.

https://doi.org/10.1016/j.gr.2022.09.002
1342-937/© 20XX

known as the Neoproterozoic Centralian Superbasin, formed at the time of break-up of Rodinia (ca. 800 Myr, Korsch and Lindsay, 1989).

The Congo basin (*CB*), also named Cuvette Centrale for its bowl shape, occupies a large part of the Congo Craton, which is composed of several Archean cratonic blocks (Ntem, Bouca-Mboumou-Uganda, Tanzanian-Kibaran, and Cuango-Kasai blocks) that collided during the Rodinia amalgamation, occurred in the Late Mesoproterozoic (Fig. 1A). The cratons are surrounded by Paleo- and *meso*- Proterozoic mobile belts (de Wit and Linol, 2015; Fernandez-Alonso et al. 2012; Boniface and Schenk, 2012). The age of the *CB* formation (late Mesoproterozoic, about 1100 Myr), older than that assumed in previous studies (Daly et al, 1992; Kadima 2011; Linol et al, 2015), is based on that of the oldest sediments recorded in one of the branches of the rift (Mbuji-Maji area) and was obtained from the interpretation of the almost 3000 km of seismic reflection profiles (Delvaux et al., 2021). Furthermore, since the extension might have started before the beginning of the sedimentation, very likely the initial *CB* subsidence preceded the Rodinia assembly (1100 Myr).

The extensional phase that produced the formation of a very heterogeneous basement, characterized by several basins and highs, NW-SE aligned (Delvaux et al., 2021; Maddaloni et al., 2021), could have been likely the effect of the action of a slow multi-divergent velocity (i.e., multi-directional extension, Gerya and Burov, 2018; Koptev et al., 2018) on a cratonic lithosphere, which have induced the initial subsidence of the *CB* in a weaker part of the craton. The amalgamation of the cratons, composing the basement of the *CB*, likely left a weak zone in the suture areas, corresponding to the central part of the *CB*, which could have been more easily deformed, under the influence of tectonic stresses (Fig. 1B).

The hypothesis that a multi-divergent velocity caused formation of complex intercepting rift patterns has been recently tested by Gerya and Burov (2018) for intra-oceanic extension to explain the generation of quadruple *rift-rift-rift-rift* and triple *rift-rift-rift* junctions, transient features, evolving in the more stable triple *ridge-ridge-ridge* junctions in few tens of Myr. However, a multi-divergent velocity could have acted also on intra-continental cratonic areas (Koptev et al., 2018) and the geometric and kinematic characteristics of the lithosphere involved in the formation of triple/quadruple junctions could have been similar to that of the lithosphere underlying intracratonic basins, such as the *CB*. Koptev et al. (2015) modelled tensional far-field stress, induced by the rise of a mantle plume beneath a cratonic area in 3D and monitored the surface topography evolution. The results showed the formation of a series of topographic highs and lows, forming parallel rift structures, due to the interaction of the plume with a lithosphere having a variable thickness and rigidity. These features are the effect of a unidirectional extension exerted by the mantle plume. In a more recent study, Koptev et al. (2018) simulated the formation of a triple junction in Central Afar as effect of a mantle plume upwelling under variable far-field stress conditions. They demonstrated that a complex pattern of rift-rift-rift triple junctions form in response of a complex multi-directional extension. Further 2D and 3D numerical studies aimed at investigating evolution of the lithosphere affected by complex extension induced by mantle plumes (e.g., Burov and Cloetingh, 2010; Gerya et al., 2015; Cloetingh et al., 2021).

Starting from these considerations, we implemented 3D geodynamic models, using the thermomechanical *I3ELVIS* code (Gerya and Yuen, 2007; Munch et al., 2020) to test the hypothesis that the complex structures of the *CB* basement are the product of a very slow multi-divergent velocity, acting on a cratonic area. The results of the numerical models are used to implement forward gravity models to estimate the temporal variations of the gravity effect of the tectonic structures formed during the simulations. Finally, we compared the forward gravity models with the present-day gravity field, in order to demonstrate the consistency between the modelled and observed main structures of the *CB*, formed during the *syn*-rift phase.

2. Numerical model

We used the 3D parallel thermomechanical numerical code *I3ELVIS*, which solves the momentum, mass and energy conservation equations for incompressible heterogeneous visco-plastic medium (Gerya and Yuen, 2007; Munch et al., 2020). The code is based on Eulerian staggered grid finite difference schemes combined with Lagrangian marker-in-cell techniques (Gerya and Yuen, 2007; Gerya, 2019).

The density for different rocks is function of temperature, and pressure (P) as:

$$\rho(T,P) = \rho_r \left[1 + \beta\left(P - P_r\right)\right] \times \left[1 - \alpha(T - T_r)\right] \quad (1)$$

where ρ_r is the reference density of a given rock at the reference pressure $P_r = 1$ bar and temperature $T_r = 298.5$ K, while α and β are the thermal expansion and compressibility coefficients, respectively.

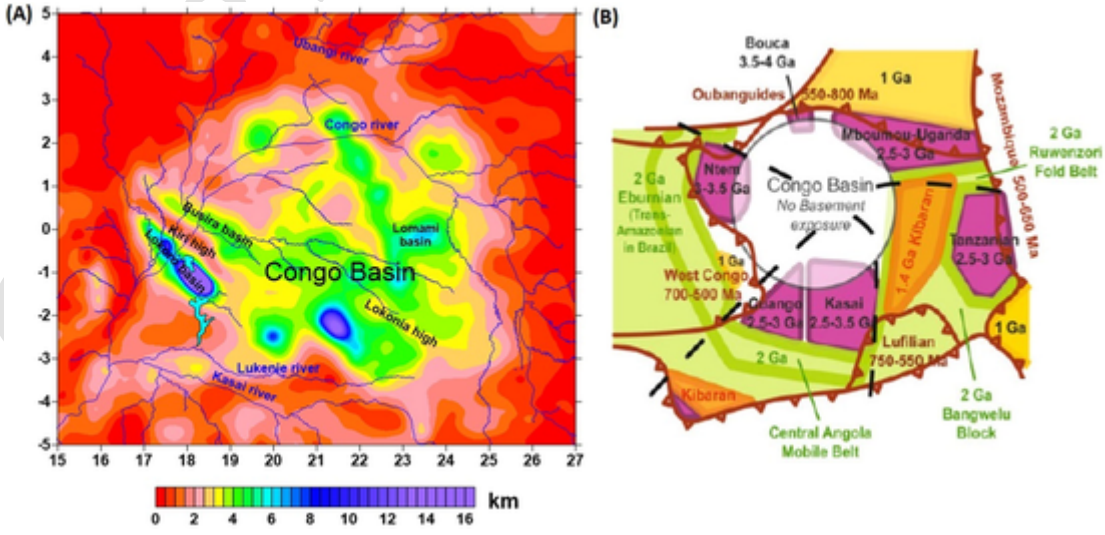

Fig. 1. Study area (A) Topography map of the Congo Basin (*CB*), using ETOPO 1 (Amante et al., 2009). (B) Sketch map of the Precambrian basement underlying and surrounding the *CB*, showing the Archean cratonic blocks (purple), Eburnian (green) and Kibaran terrains (orange and yellow). Brown curves represent the tectonic fronts of Pan African fold-and-thrust belts. Dashed black lines show the possible suture zones of the amalgamated cratonic pieces (modified from de Wit and Linol, 2015).

Our rheological model accounts for the visco-plastic rocks deformation, using an effective creep viscosity ($\eta_{ductile}$) that combines diffusion (η_{diff}) and dislocation creep (η_{disl}) viscosity:

$$\frac{1}{\eta_{ductile}} = \frac{1}{\eta_{diff}} + \frac{1}{\eta_{disl}} \tag{2a}$$

$$\text{with } \eta_{diff} = \frac{A_D}{2\sigma_{cr}^{n-1}} \exp\left(\frac{E+PV}{RT}\right)$$

$$\eta_{disl} = \frac{A_D^{1/n}}{2} \exp\left(\frac{E+PV}{RT}\right) \dot{\varepsilon}_{II}^{\frac{1}{n}-1} \tag{2b}$$

where A_D, E, V, experimentally determined and considered as a constant, are the pre-exponential factor, the activation energy and volume, respectively. R is the gas constant, P the pressure, T the temperature, $\dot{\varepsilon}_{II}$ the second invariant of the deviatoric strain rate tensor, and σ_{cr} is the diffusion-dislocation transition stress (named critical stress in Table S1.1, Supplementary Material S1). Cutoff limits of 10^{18} Pa s and 10^{26} Pa s were applied to limit minimal and maximal rock viscosity, respectively.

The plastic strength (σ_{yield}) of rocks depends on pressure (P) as:

$$\sigma_{yield} = C + \sin(\varphi)P \tag{3}$$

where C is the compressive strength at $P = 0$, φ is the effective internal friction angle.

Our largest model domain covers a volume of 4050 × 392 × 4050 km^3, that is resolved by 405 × 197 × 405 grid points, with a resolution of 10 × 10 km in the horizontal (x-z) plane and 2 km in the vertical (y) direction. Higher resolution in vertical (2 km) compared to horizontal (10 km) direction is used to properly resolve vertical thermal-rheological structure of the lithosphere and crust (Fig. 2 c-d). The large horizontal dimensions of the model area are chosen to be greater than these of the Congo craton, to minimize effects of boundary conditions on intra-cratonic deformation. It should also be noted that the aim of these simplified numerical simulations is to understand the tectonic conditions that lead to the formation of a heterogeneous basement depth, characterizing the *CB* (Delvaux et al., 2021; Maddaloni et al., 2021), without performing a detailed quantitative comparison with natural data. Since there is a lot of uncertainty about the initial shape and structure of the Congo Craton, we implemented several models, in which the study area is composed of cratonic lithosphere divided by (or containing) 'weak zones', having different lithospheric thickness and thermal structure. More precisely, in one model setup, we assumed that the amalgamation of cratonic pieces resulted in four cratonic blocks, divided by two intercepting narrow weak zones crossing each other in the central part of the model. In all the other simulations, we assumed that the collision of the cratonic pieces simply left a weak, warm and fertile rectangular lithospheric zone in the center of the model. In all cases, the transition between the lithosphere of cratons and weak zones is prescribed to be smooth through "transition zones" (*TZs*) (Fig. S1.1, Supplementary Material S1).

We considered a fixed initial crustal thickness of 35 km, divided in an upper and lower crust of 20 km and 15 km, respectively, and a fixed lithospheric thickness in the cratonic areas equal to 230 km, in agreement with the estimates derived from seismic tomography data (e.g., Emry et al., 2019; Celli et al., 2020). Depth temperature variations in the cratonic areas are defined by a linear gradient between 273 K at the surface topography and 1698 K at the bottom of the lithosphere. The areas off-cratons (weak zones) and the *TZs* have a different depth of the lithosphere and thermal gradient for each numerical simulation. Assuming that *CB* formed in the Precambrian time, we used warmer mantle potential temperature than present day value (1573 K) and took into account the increase of adiabatic temperature with depth (0.5 K/km) to define mantle temperature at LAB at different depths under both on-craton and off-craton areas (Fig. 2c). Below the LAB, the temperature increases adiabatically (~0.5 K/km), reaching at the bottom of the model (392 km) a temperature of 1973 K. The use of linear temperature gradient neglects effects of radiogenic heating in the crust. We used this model simplification since our study aims at investigating first order effects that the mantle uprising has on the lithospheric structures of cratonic areas. We also do not model melting and melt extraction, since the outcropping volcanic products in the *CB* are limited both in space and time (Delvaux et al., 2021). Indeed, melt extraction and upward transport, which produce lithospheric weakening and crustal growth by magmatic processes (e.g., Gerya et al., 2015, Koptev et al., 2021), are more abundant when the tectonic extension is caused by a plume (e.g., Gerya et al., 2015).

In order to simulate a slow multi-extensional tectonics, we applied symmetrical bi-divergent velocity boundary conditions (2.5 mm/yr, half-rate) in N—S and E-W direction, along the nodes of the lateral boundaries of the model. The velocities applied at the top and bottom of the model (0.05 and −0.85 mm/yr, respectively) satisfy the condition of the global mass conservation. To allow surface deformation, the free-surface boundary condition at the top of the crust is implemented by using a 20 km thick *sticky air* layer (Crameri et al., 2012) with low density (1 kg m^{-3}) and low viscosity (10^{18} Pa s).

The reference density (ρ_r) of the cratonic lithosphere is assumed lower (3250 kg/m^3) than that of the more fertile off-cratonic areas and asthenosphere (3300 kg/m^3), since the melt-depletion in iron components characterizing the Archean rocks makes them more buoyant (McDonoug and Sun, 1995; Poudjom et al., 2001). We assume the rheology of the dry olivine for both lithospheric and sublithospheric mantle, while felsic and mafic granulite for the upper and lower crust, respectively (Ranalli, 1995). The rheological and thermo-physical parameters with the values assumed in the numerical simulations are displayed in Table S1.1 (Supplementary Material S1).

3. Numerical results

In our models, we investigate the differences in the tectonic features formed, depending on the lithospheric thickness, size, and thermal gradient of the off-cratoninic areas (weak zones). In Table 1, we describe parameters of different numerical experiments, in terms of their geometry design and bottom temperature applied to the crust and mantle lithosphere of the weak zones, together with the simulation time, spanning from 50 Myr to 200 Myr. The upper time limit was chosen considering that the rift duration is supposed to have lasted maximum 200 Myr (Delvaux et al., 2021).

In the next sections, we discuss the results of the two reference simulations that differ strongly in term of their geometry design and initial temperature conditions (1_Congo_weak1 and 2_Congo_weak2).

3.1. Reference model 1_Congo_weak1

Numerical model design: The numerical simulation has been conducted considering the existence of a weak zone of size 405 × 405 km (*1_Congo_weak1*, Fig. 2a), located in the central part of a single cratonic block, surrounded by *TZs* of size equal to 101 km. The depth of the lithosphere in the weak zone is of 180 km and the distance between the weak zone and cratonic borders is 1822 km.

Initial Temperature Conditions: According to the geometry above described, in the areas external to cratonic blocks, we associated a temperature at the base of the crust and mantle lithosphere of 773 K and 1673 K (Table 1), respectively. We chose these values, in order to obtain a crustal gradient, which is more than double (~14 K/km) than that of the mantle lithosphere (~6 K/km), as displayed in Fig. 2c). This setup favors rheological decoupling of the crust from the mantle lithosphere in the weak off-craton zone, and thus a more distributed deformation (Fig. 2c). In contrast, in the cratons, where the cold temperature gradient (~6 K/km) is applied in the entire lithosphere, rheological coupling of the lithospheric layers occurs (Fig. 2c-d).

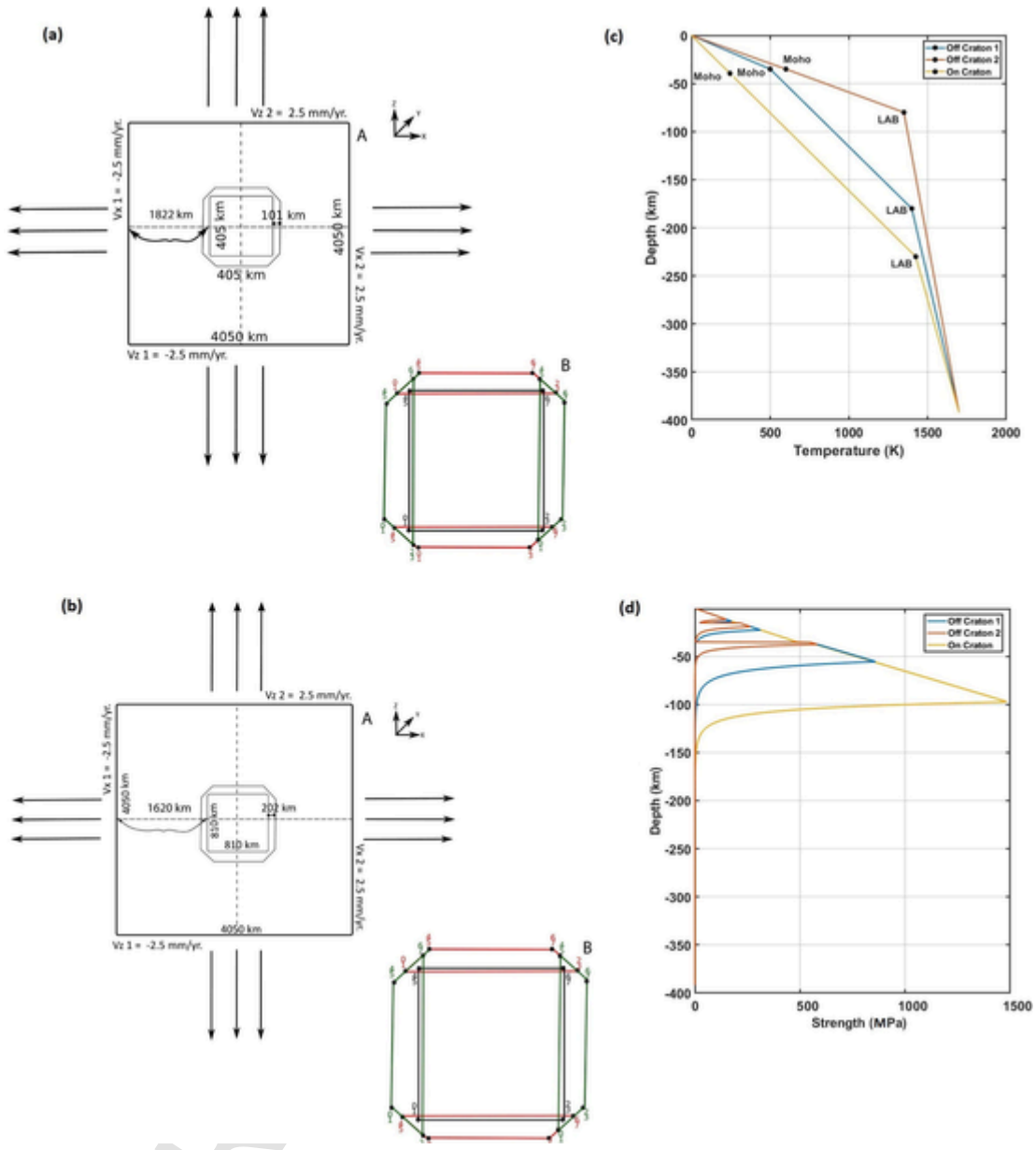

Fig. 2. Geometry design of the model **(a)** 1_Congo_weak1 and **(b)** 2_Congo_weak2. **A**: Horizontal plane visualization of the model. Black arrows show velocity directions. **B**: Zoom in plan on the weak zone (black square), represented in staggered-in cell marker technique. Red and green features represent the *TZs* and numbers are as in Fig. S1.1. Initial geotherms **(c)** and strength envelopes **(d). On craton**: Geotherm and strength envelope of the cratonic areas. **Off craton 1**: First end-member geotherm and strength envelope of the areas outside the cratons, having a lithospheric thickness of 180 km and a temperature at the Moho and base of the lithosphere depth of 873 and 1623 K, respectively. **Off craton 2**: Second end-member geotherm and strength envelope of the areas outside the cratons, having a lithospheric thickness of 80 km and a temperature at the Moho and base of the lithosphere depth of 773 and 1673 K, respectively (see Table 1). **Moho**: Boundary layer between lower crust and upper mantle. **LAB**: Lithosphere-Asthenosphere Boundary.

3.1.1. Main results

Temporal variations of the surface topography (Fig. 3) show a progressive subsidence along two elongated zones, which compose two perpendicular rift structures that intersect in a quadruple junction between 50 and 100 Myr (Fig. 3a-c). These structures are effect of the upwelling of the asthenosphere that increases the size of the thermal anomaly and enhances lateral contrast in temperature and lithospheric thickness variations (Figs. 4-6). The progressive asthenospheric uprising produces a well-defined updoming of the base of the lithosphere below the two rift structures (lithospheric thinning), between 100 and 200 Myr and of the Moho depth in the central part of the model (Figs. 4-5).

This is even more visible looking at the cross-sections that display the temporal depth-viscosity variations, where we observe the upwelling of low viscosity zone, corresponding to the thermal anomaly, at the Moho depth (Fig. 7). Lateral viscosity variations (Figs. S1.2-S1.4, Supplementary Material S1) show more clearly, along the two rift structures, the viscosity decrease at the lithospheric depths, due to the asthenospheric uprising and a progressive viscosity increase at the Moho depth, due to the replacement of the lower crust with mantle material. The response of the surface topography to these processes consists in the formation of a central depression and in the uplift of the edges of the two rift zones (Fig. 3d). Therefore, the geometry design used in this simulation produces a heterogeneous basement depth, characterized by an alternation of highs and depressions in a central subsided circular zone.

Table 1
Parameters of performed numerical experiments. *The depth is referred to the surface topography.

Models	Model size (km)	Depth Litho (weak zone) (km)	T. Moho (weak zone) (K)	T. Litho (weak zone) (K)	Simulation Time (Myr)
1_Congo_cratons	1900 × 1900 (Cratonic Block)	180	773	1673	95
1_Congo_weak1	405 × 405 (Weak Zone)	180	773	1673	200
2_Congo_weak2	810 × 810 (Weak Zone)	80	873	1623	200
3_Congo_weak3	810 × 810 (Weak Zone)	80	873	1623	50
4_Congo_weak4	405 × 405 (Weak Zone)	80	873	1623	200
1_Congo_ cratons + weak	1402 × 1402 (Cratonic Block) 623 × 623 (Weak Zone)	80	873	1623	100

3.2. Reference model 2_Congo_weak2

Numerical model design: As in the previous numerical simulation (*1_Congo_weak1*), we considered the existence of a weak zone in the central part of a single cratonic block, but in this case twice extended (810 km × 810 km) and having a lithospheric thickness of 80 km. The *TZs* have the size of 202 km and the distance between the weak zone and the craton borders is 1620 km (*2_Congo_weak2*, Fig. 2b).

Initial Temperature Conditions: Since we assumed that the lithosphere of the weak zone is twice times thinner than in the model 1_Congo_weak1, we increased the thermal gradient both in the crust and mantle lithosphere to ~ 17 K/km (Fig. 2c1), associating a temperature at the bottom of the crust and lithosphere of 873 K and 1623 K, respectively (Table 1). This higher thermal gradient is more consistent with a thinner lithosphere, representing the suture zone between the cratonic blocks. As a consequence, the decoupling between the crust and mantle lithosphere occurs at a shallower depth, compared to the previous model (Fig. 2c-d).

Main Results: The results are similar to those observed in the previous simulation (1_Congo_weak1). However, the increase of the size of the weak zone and decrease of its lithospheric thickness produces a larger depressed central zone and promotes an earlier formation of the two rift structures, with well-developed flanks already at the time step 100 Myr. Further uplift occurs in the central part of the two rifts at 200 Myr. We can notice that in these areas both the Moho and lithosphere-asthenosphere depths are uplifted (Figs. 9-10), as in the previous simulation. The formation of these features is the direct effect of the asthenospheric upwelling under a greater weak zone (Fig. 11). As for the previous model (1_Congo_weak1), these features are also observable looking at temporal depth and lateral viscosity variations at different time steps (Fig. 12 and S1.7-S1.11, Supplementary Material S1).

4. Interpretation of numerical models results

The numerical models displayed in the previous section, show how the different geometry designs and initial temperature conditions could influence the upwelling of the asthenospheric mantle, causing variations in temperature, viscosity and density, and thus in the surface topography. However, the two simulations, show some commonalities in the structures formed. In particular, the application of a multi-divergent velocity produces in both cases a circular subsided zone in almost all the early stages of the simulations. This almost rounded area increases its size with time, while its topography is affected by significant variation (Supplementary Material S2A and S2B). For these reasons, it can ideally represent the *CB* and its heterogeneous basement, characterized by a series of topographic highs and depressions. Furthermore, the maximum subsidence of the surface topography is reached, after a time lapse between 50 and 100 Myr, along two elongated structures, orthogonal each other, representing two rift zones intersecting in the centre. These zones are characterized by a low viscosity at the base of the lithosphere and Moho. On the other hand, at the time step 200 Myr, along the same zones, we observe an increase of viscosity at the Moho depth, due to the replacement of the crust with mantle material, and an initial uplift of the surface topography induced by the uprising of the asthenosphere at crustal depths. We can notice that these features, in the model 2_Congo_weak2 form 50–100 Myr before than in 1_Congo_weak1. In particular, the edges of the two rift structures initiate to uplift at their corners already at the time step 50 Myr in model 2_Congo_weak2 and are completely uplifted at 100 Myr. This stage of deformation is reached only at 200 Myr in model 1_Congo_weak1. These rift structures converge in a quadruple junction and are similar to the intercepting oceanic rifts formed in the numerical experiments of Gerya and Burov (2018). However, the set-up and boundary conditions of their models is quite different from those of our simulations, since much higher multi-divergent velocity rates (within the range 0.5–3.5 cm/yr) are applied to a relatively thin and young oceanic lithosphere (30 km thick), in which a 2 × 2 × 2 km highly strained region (weak inclusion) in the lithospheric mantle at 13 km depth, is prescribed. The quadruple junctions form in all their numerical experiments as transient features, that, according to the higher multi-divergent velocity applied, rapidly (in < 1 Myr) migrate and evolve in the more stable triple junctions formed during the oceanic spreading stage. In our models, the two rift structures, marked by a significant different viscosity and topography with respect to those of surrounding areas, appear as stable long-lived features, becoming evident between 0.010 and 50 Myr and persisting for > 100 Myr, with a gradual increase of their length. The longevity of these rifting structures is likely a consequence of slower extension rates and thicker continental lithosphere used in our models compared to Gerya and Burov (2018) experiments. We can also observe that even if the initial lithospheric thickness in the weak zone differs between the two models of 100 km, the Moho depth, at the time step 200 Myr, in the central part of the models, differs of only few kilometers (Figs. 4 and 9), while the lithospheric depth of about 10 km (Figs. 5 and 10). This means that the mantle updoming tends significantly to slow down when the asthenosphere arrives at shallow depth (~60 km depth), probably due to the higher buoyancy of the upper lithosphere.

In order to identify further possible similarities and differences between the modelling results and main structures of the *CB*, we draw three main cross-sections along the surface topography obtained at the time step 200 Myr and compared their trends with that of the basement depth reconstructed from the interpretation of seismic reflection data (Delvaux et al., 2021). In doing such a comparison, we should consider that the basement depth, after the first stage of extension, has been further modified by successive compressional tectonics, related to the Gondwana assembly at the beginning of the Paleozoic and far-field intraplate compression at the Triassic-Jurassic transition (Delvaux et al., 2021). In addition, also the load variation induced by the sedimentation and erosion that accompanied the tectonic processes and enhanced by the climatic changes, contributed to modify the basement depth.

Looking at Fig. 13, we can observe that the cross-section A-B, passing through one of the two rift structures, shows a subsided area, with an uplift in the centre in model 1_Congo_weak1, while the same area is characterized by less subsidence and small topography perturbations in model 2_Congo_weak2. In contrast, along the profile C-D, 45° oriented with respect to the first profile, the situation is reversed (Fig. 13). On other hand, the edges of the central depressed area are moderately and strongly uplifted in model 1_Congo_weak1 and 2_Congo_weak2, respectively. Therefore, both models can simulate the formation of a de-

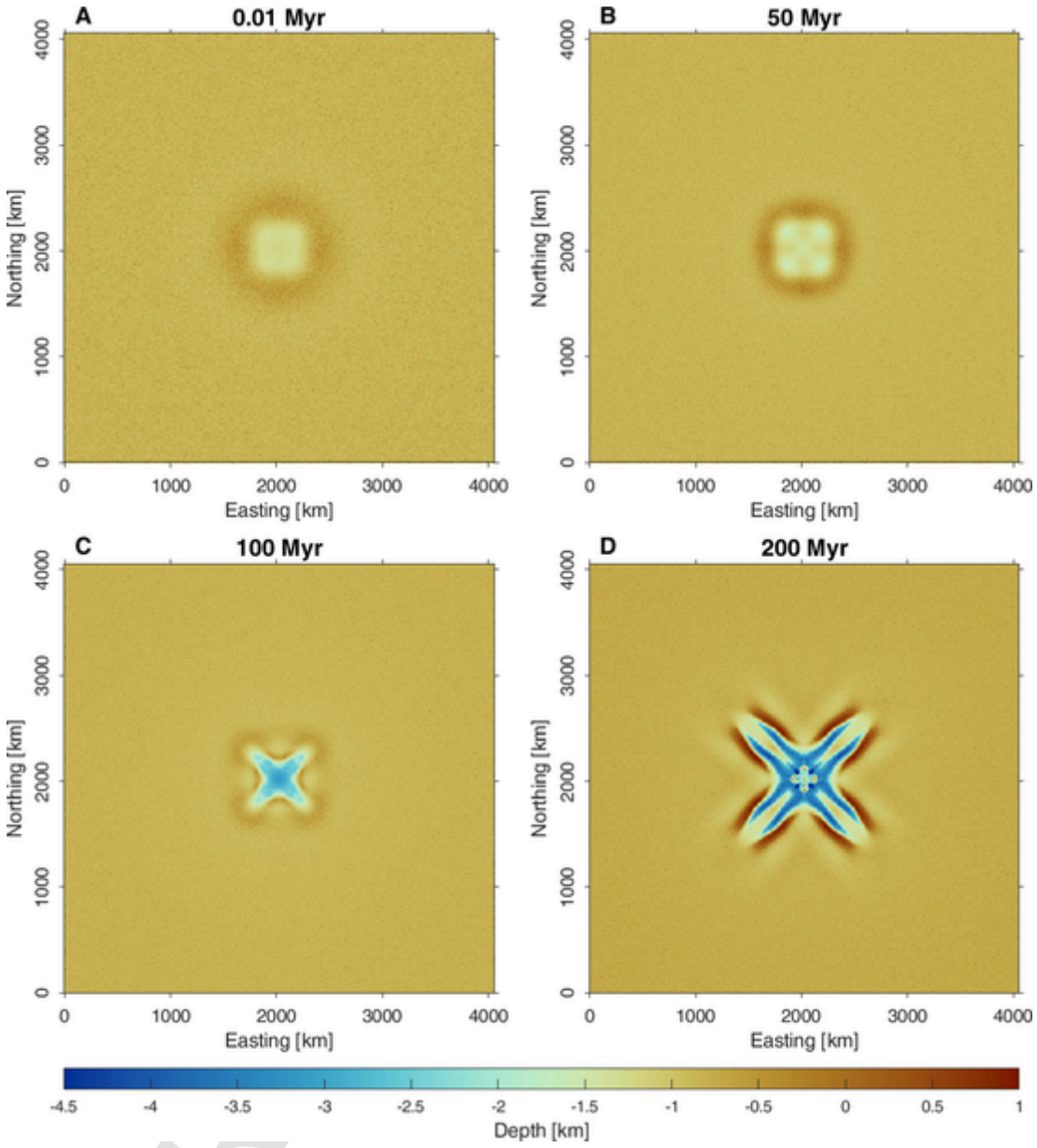

Fig. 3. Model 1_Congo_weak1. Lateral variation of surface topography (m) at 0.010Myr (**A**), 50 Myr (**B**), 100 Myr (**C**), and 200Myr (**D**). The topography reference value is −1 km.

pressed central area of different size, fragmented by minor lows and highs, along one preferential direction and limited by uplifted edges.

Furthermore, the surface topography in both models varies sharply of 2–3 km within a distance of ~100 km, along a cross-section perpendicular to the orthogonal structures (E-F, G-H). This demonstrates that the deformation induced by the multi-extensional stress can affect also areas far from the centre. As we discussed in Delvaux et al. (2021), the basement depth of the *CB* is very heterogeneous, flooring a large circular depression, characterized by an alternation of lows and highs, NW-SE oriented as those of Bololo Basin, Inongo High, Lokoro Basin, Kiri High, Busira Basin, and Lulonga High (profile 1, Fig. S1.12, Supplementary Material S1**)**, as well as the Gilson and Samba basins, separated by the accommodation zone of the Kiri and Lokonia Highs (profile 2, Fig. S1.12, Supplementary Material S1). This alternation resembles that reproduced by the two simulations considered, along the cross-section A-B (2_Congo_weak2) and C-D (1_Congo_weak1) of Fig. 13 and thus can be partly ascribed to a multi-extensional tectonics that by acting on the Congo Craton, produced a rift phase during the Mesoproterozoic age.

The resulting basement depth variation is represented in both simulations by the sharp topography change characterizing the central subsided area. On the other hand, the flat subsided area with a high peak in the centre, observed along cross-section A-B (1_Congo_weak1) and C-D (2_Congo_weak2) of Fig. 13 resembles the shape of the Maringa ridge limiting the Lomami Basin (Maddaloni et al., 2021). The transition to the uplifted zones, bordering the subsided central area along the AB and CD profiles, reminds the surface topography variation between the Dekese basin and Lokonia High, shown along profile 3 of Fig. S1.12 (Supplementary Material S1).

Looking at the lateral density variations at the base of the lithosphere, at the time steps 0.010 Myr and 200 Myr (Figs. 14–15), we observe that both models are initially characterized by a central area having density lower than surroundings that induces initial topography perturbations (Fig. 14A, 14C 15A, and 15C). At 200 Myr, the updoming of the hot asthenosphere in the central part of the model causes a den-

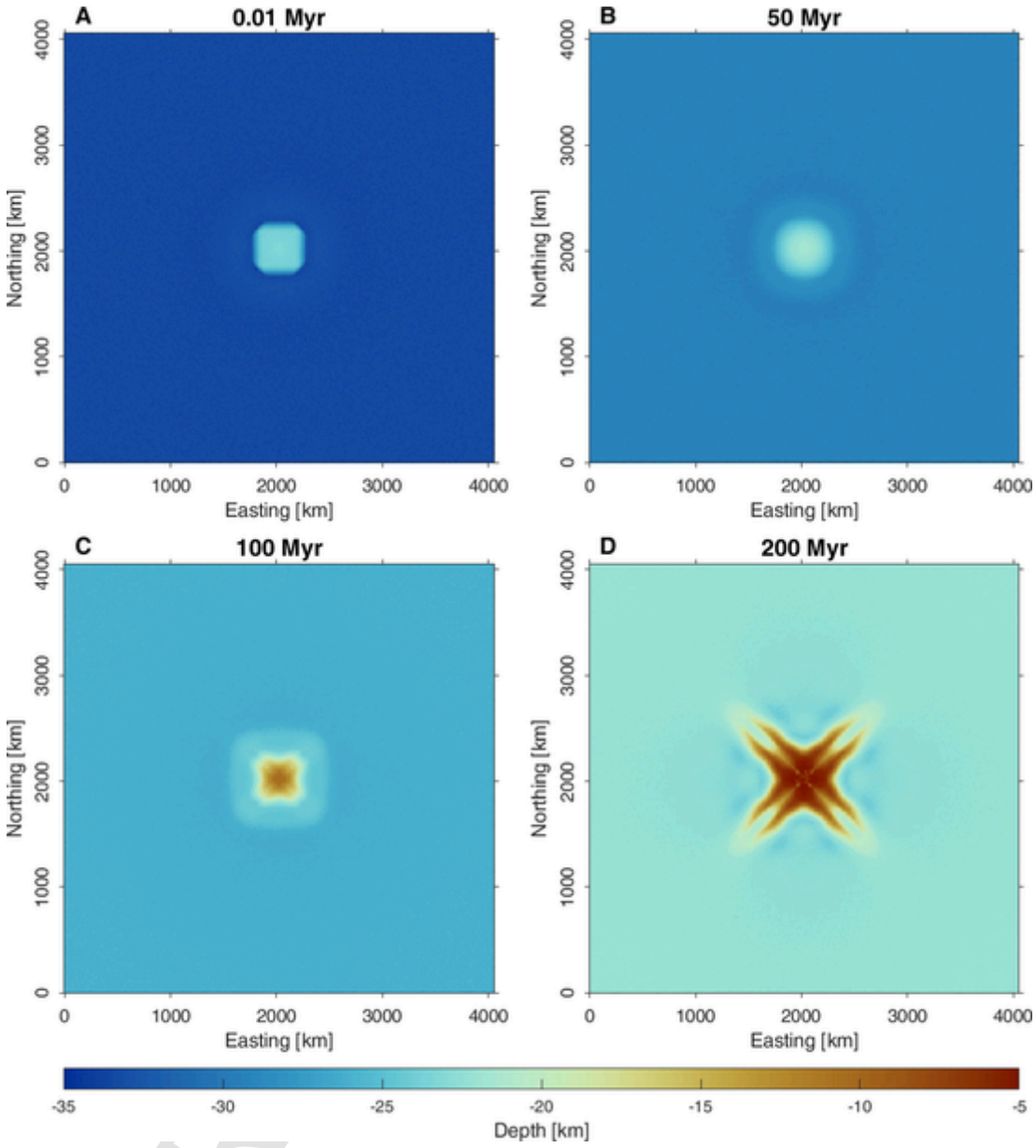

Fig. 4. Model 1_Congo_weak1. Lateral variation of the Moho topography (m), defined by the depth of the isodensity 3000 kg/m^3, at 0.010Myr (**A**), 50 Myr (**B**), 100 Myr (**C**), and 200Myr (**D**). The topography reference value is −35 km.

sity decrease at the bottom of the lithosphere along the two rift structures (Fig. 14B, 14D-D', 15B, and 15D-D'). These features overprint a circular zone of higher density, produced by a slower, and thus less hot, mantle upwelling (Fig. 14B and 15B). The described structures have a larger size in model 2_Congo_weak2, due to the larger geometry design and different initial temperature conditions assumed.

The temporal density variations produce a surface topography depression in the central part of the model, interrupted by sharp uplifts in the model 1_Congo_weak1, indicating strong lateral density changes within the subsided area. In contrast, in the model 2_Congo_weak2, there is only an uplift in the centre of a much larger topography depression, due to the upraised hot asthenosphere. In both models, the central subsided area forms consequently to the replacement of the less dense more buoyant cratonic lithosphere with the denser asthenosphere, which cools migrating far from the centre. On the other hand, the sudden surface topography increase, at the edges of the subsided area, sharply occurs in correspondence of the lateral lithospheric density variations, accompanying the depth changes of the Moho and bottom of the lithosphere, at the transition from the deformed central area to the almost stable and stiffer external cratonic part. The edges are more uplifted in model 2_Congo_weak2, in correspondence of the thickening of the low-density part of the lithosphere and increase of the Moho depth. We can further notice that the lateral density variations, occurring in the more peripheral parts of the model during the extensional deformation, does not significantly affect the initial surface topography ($< \pm 1$km variation).

5. Influence of model parameters

As displayed in Table 1, we performed other numerical simulations with different geometry design and or initial temperature conditions with respect the two models discussed. We display the short description of the geometry design, initial temperature conditions, and results of these additional models in the Supplementary Material S3. The first numerical model implemented (1_Congo_cratons), composed of four cratonic blocks divided by weak zones crossing in the central part of the

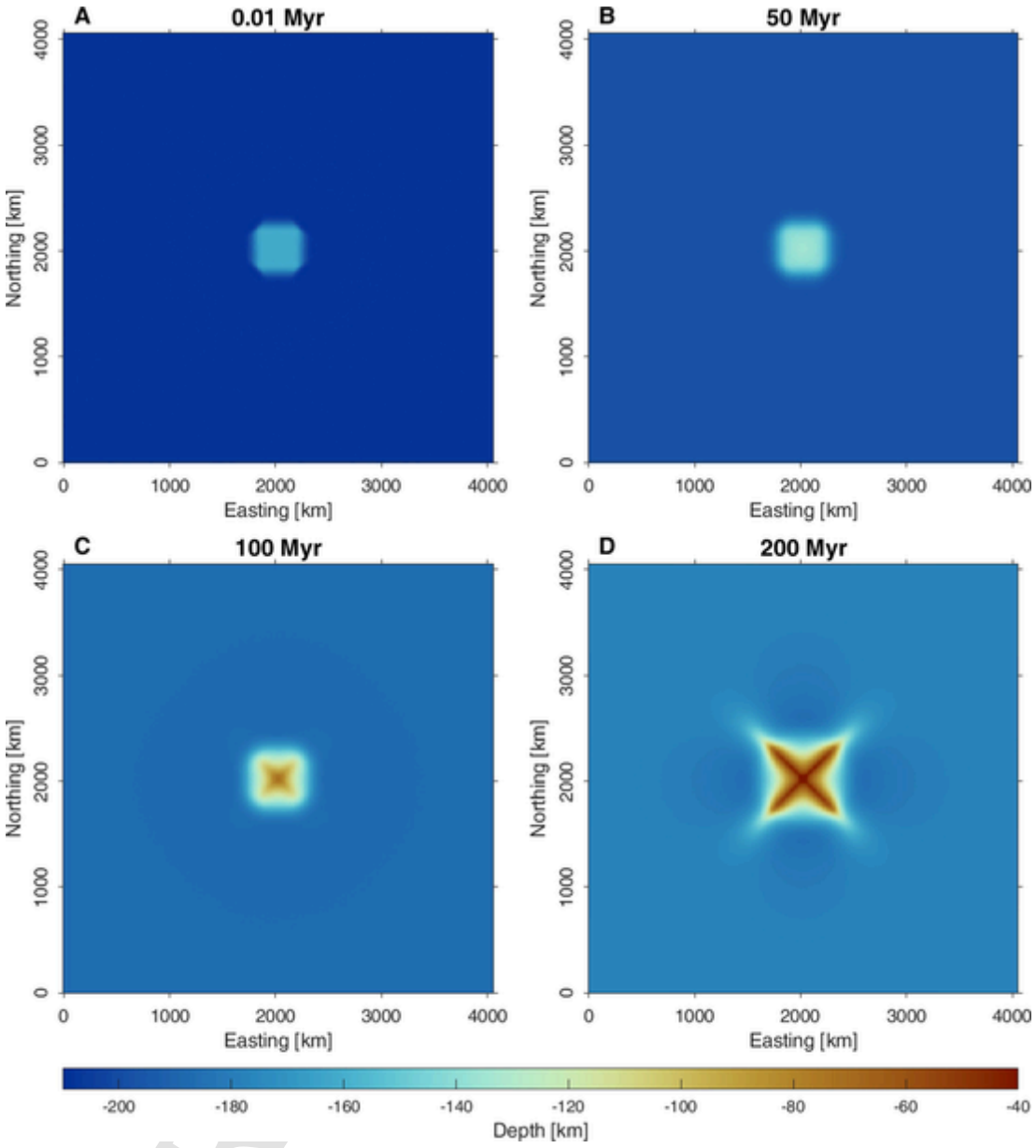

Fig. 5. Model 1_Congo_weak1. Lateral variation of topography (m) of the lithosphere-asthenosphere thermal boundary, defined as depth of the isotherm 1573 K (typical present-day reference value), at 0.010Myr (**A**), 50 Myr (**B**), 100 Myr (**C**), and 200Myr (**D**). The topography reference value is −210 km.

model (Fig. S3.1, Supplementary Material S3), produces unrealistic results, consisting in a greater subsidence in the area between two adjacent cratons than in the central part of the model and uplift of the cratonic edges (Fig. S3.2, Supplementary Material S3), where we observe a localized upwelling of the asthenosphere (Fig. S3.4, Supplementary Material S3). On the other hand, 3_Congo_weak3 and 4_Congo_weak4 models (Figs. S3.5 and S3.16, Supplementary Material S3) produce results similar to those already discussed (Figs. S3.6-S3.15 and Figs. S3.17-S3.26, Supplementary Material S3). In particular, 3_Congo_weak3 has the same geometry and initial temperature conditions of 2_Congo_weak2 model, but a different orientation of the weak zone (its vertices are 45° rotated with respect to those of the other models) and the *TZs* between the cratonic and not cratonic lithosphere are absent (Fig. S3.5, Supplementary Material S3). Since the results of this numerical test compared to the reference models show just a difference in the shape of the asthenospheric upwelling, without further effects on the topography and viscosity variations (Figs. S3.6-S3.14, Supplementary Material S3), we stopped the run at 50 Myr. In contrast, model 4_Congo_weak4, characterized by the same size of the weak zone of 1_Congo_weak1 and having a lithospheric thickness equal to that of 2_Congo_weak2, shows structures very similar to those of 2_Congo_weak2 (Figs. S3.17-S3.26, Supplementary Material S3). However, they form with a temporal delay of about 50 Myr, since the initial size of the central weak zone influences the speed of the deformation. In particular, such a delay occurs when the size of the weak zone is reduced to half of that of the reference model 2_Congo_weak2. The shape of the structures that formed in the central depressed area instead strongly depends on the initial lithospheric thickness and temperature conditions applied. Furthermore, we implemented a 'hybrid' model (1 Congo_cratons + weak), composed of four cratonic blocks and a weak zone in the centre, which are separated by a lithosphere having a depth and bottom temperature intermediate between these two types (Fig. S3.27, Supplementary Material S3). The results show again the formation of the two rift structures, showing well pronounced surface topography depression and uplift of the Moho and lithosphere-asthenosphere boundary depths already at time step 50 Myr (Figs. S3.28–3.30,

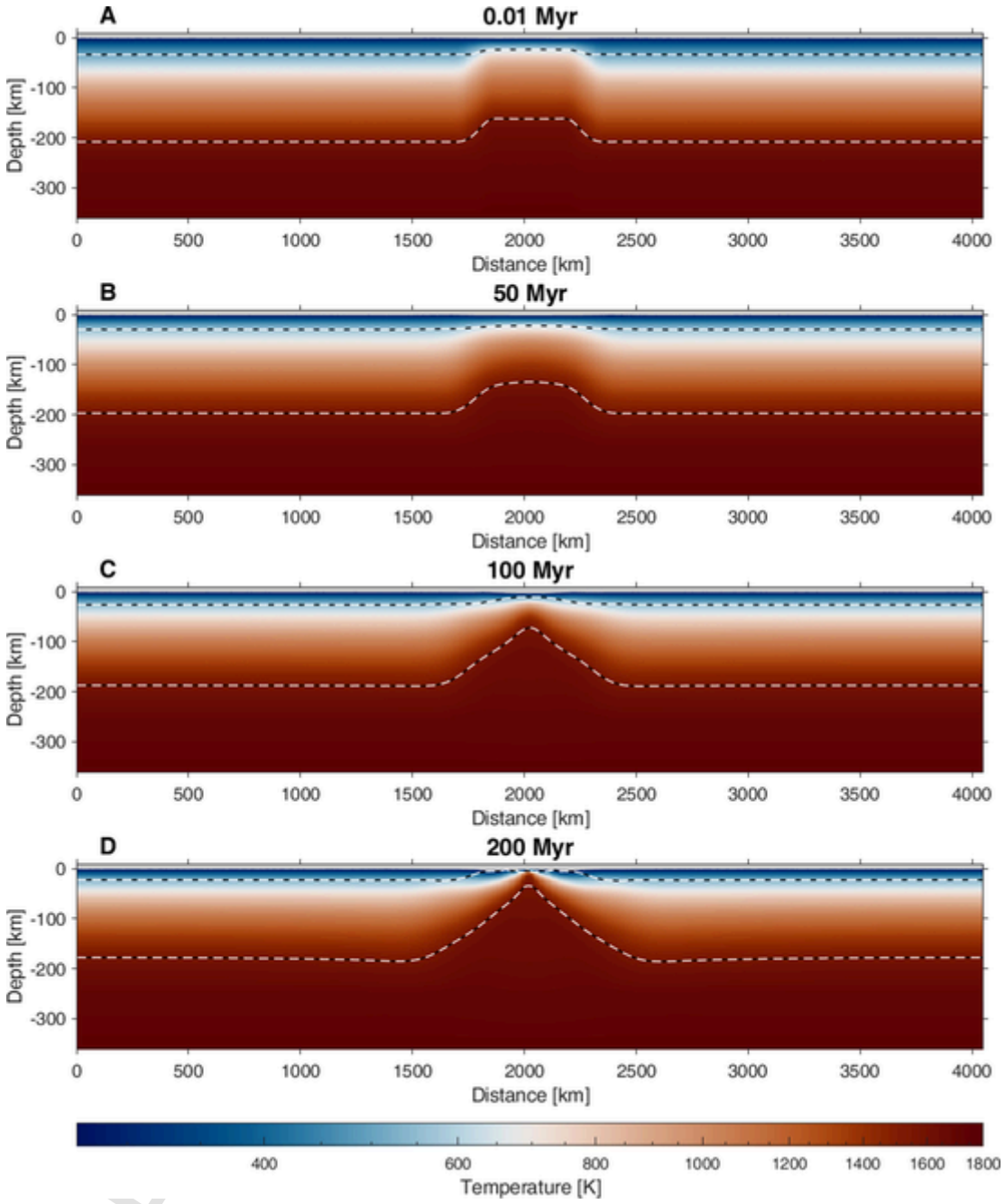

Fig. 6. Model 1_Congo_weak1. Depth-temperature variations (K) along a N—S cross-section through the model centre displayed in Fig. 14, at 0.010 Myr (**A**), 50 Myr (**B**), 100 Myr (**C**), and 200 Myr (**D**). Black-white dashed lines show the Moho depth, defined as the depth of the isodensity 3000 kg/m^3, and the depth of the lithosphere and asthenosphere boundary (LAB), defined as depth of the isotherm 1573 K (typical present-day reference value). Vertical scale is increased by 100 % with respect to the horizontal axis.

Supplementary Material S3). Their size significantly increases at 100 Myr, going beyond the limits of the circular depressed area. These features are effect of the presence of a lithosphere having an 'intermediate' structure between that of the weaker central part of the model and more rigid cratonic blocks (Fig. S3.27, Supplementary Material S3). However, the extensional stress produces uplift of the edges of the cratonic blocks, as in another model composed of four cratons (Fig. S3.2, Supplementary Material S3). Since the shapes of the structures formed are not so much consistent with those of the *CB* basement depths, we have not further analyzed the obtained results.

6. Forward gravity models setup

After performing the 3D simulations to test the hypothesis of the *CB* formation as a multi-extensional rift within a cratonic area, we calculated their gravity fields and compared them with the gravity observations. Indeed, even if the present-day gravity field reflects the superposition of the all processes that determined the current shape of the *CB*, the observed gravity anomalies pattern, consisting of an alternation of negative and positive values, is typical of a rift structure (Maddaloni et al., 2021), being identified also in other parts of the World (East and Central African Rift System).

To this aim, we performed static and dynamic forward gravity modelling (SFGM and DFGM), using the 3D numerical simulations 1_Con-

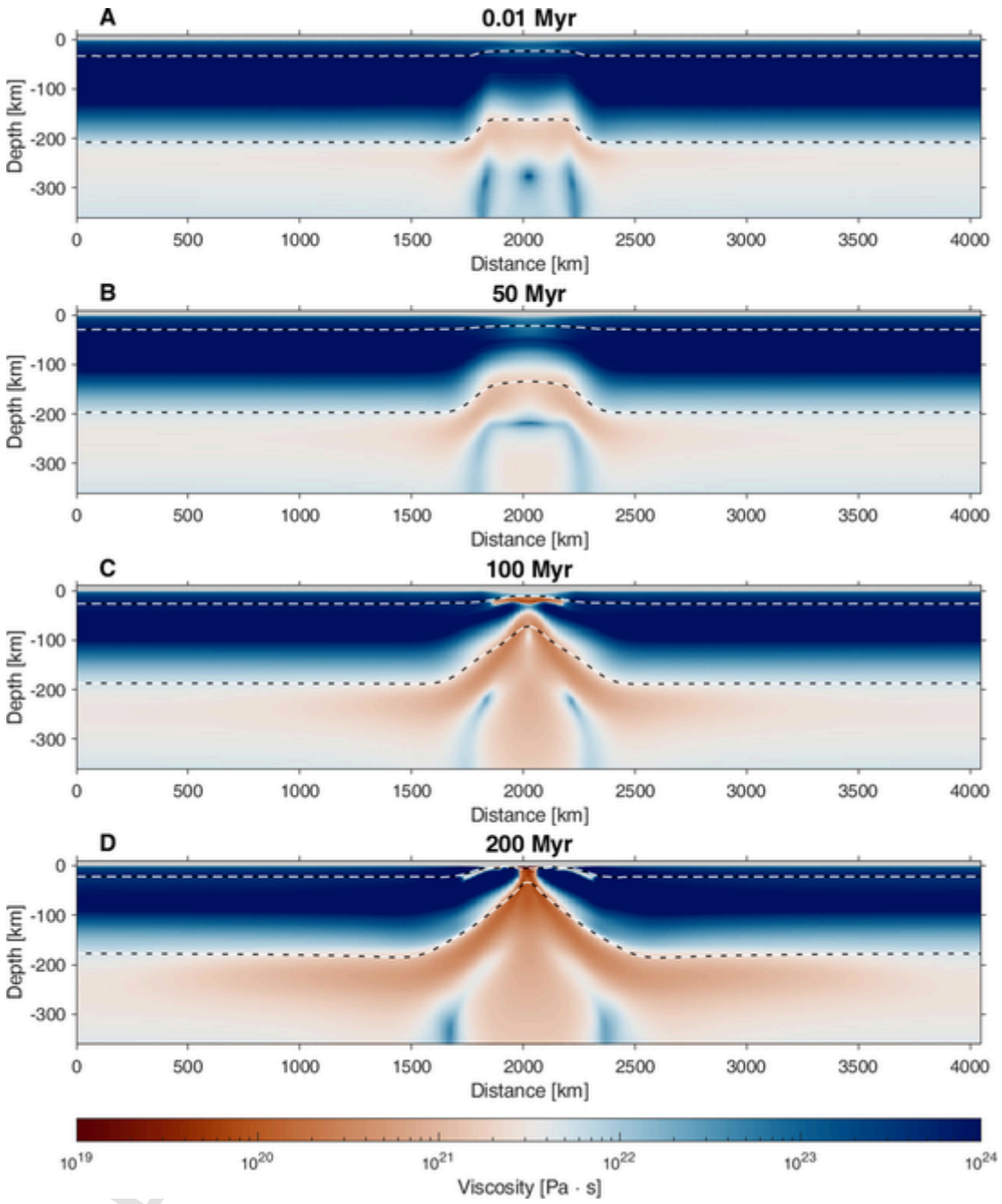

Fig. 7. Model 1_ Congo_weak1. Depth-viscosity variation (Pa s) along a N—S cross-section through the model centre displayed in Fig. 14, at 0.010Myr (**A**), 50 Myr (**B**), 100 Myr (**C**), and 200 Myr (**D**). Black-white dashed lines show the Moho depth, defined as the depth of the isodensity 3000 kg/m^3, and the depth of the lithosphere and asthenosphere boundary (LAB), defined as depth of the isotherm 1573 K (typical present-day reference value). Vertical scale is increased by 100 % with respect to the horizontal axis.

go_weak1 and 2_Congo_weak2, whose surface topography best approximates the basement depth reconstructed in Delvaux et al. (2021) and Maddaloni et al. (2021). Indeed, since the 3D numerical simulations do not include the effects of the sedimentation, the modelled surface topography has been considered as the top of the basement. The forward gravity models have been implemented using the density values computed at the Cartesian coordinates for each 3D numerical simulation. For this purpose, we constructed rectangular prisms with the center coincident to each grid point of the numerical models and length, width, and height equal to the half of the inter-node spacing. We computed the gravity effect of the models using Tesseroids software (Uieda et. al, 2016). In order to smooth the short-scale near-surface density variations, the gravity is computed at 24 km above the reference topography. Furthermore, we excluded from the computation the prisms modelling the sticky air layer, considering only those having density values > 1000 kg/m^3.

Dynamic forward gravity modelling (DFGM): This model has been implemented by computing the difference between the gravity effects of the two numerical models (1_Congo_weak1 and 42_Congo_weak2), at the time step 200 Myr, with those produced at 0.010 Myr, in order to observe how the gravity field changed over time. We have not used the difference with respect to the starting situation (time step 0 Myr), since the above illustrated numerical solutions have been shown starting from the time step 0.010 Myr.

Static forward gravity modelling (SFGM): This model has been implemented to observe the gravity anomalies, resulting from the gravity ef-

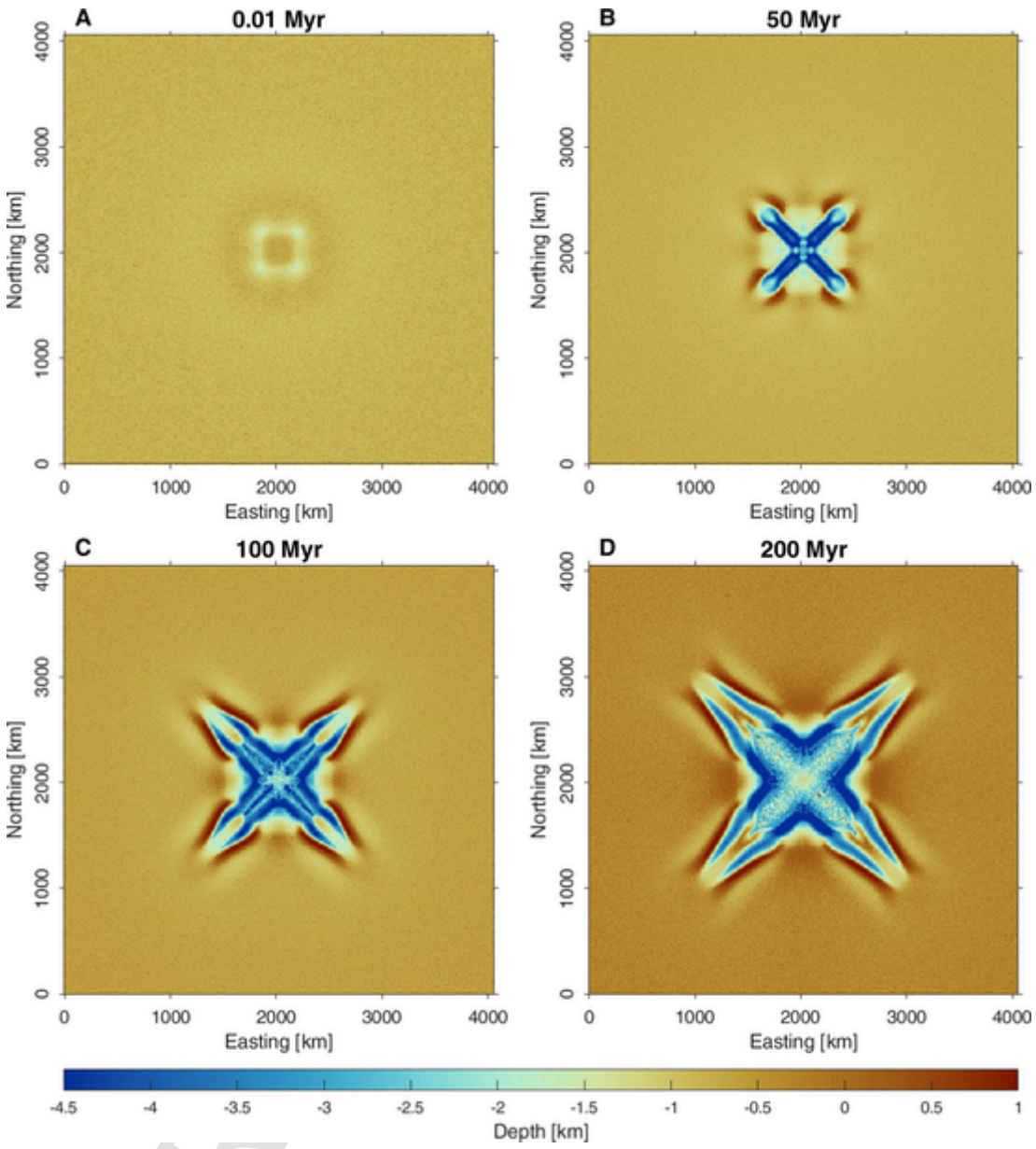

Fig. 8. Model 2_Congo_weak2. Lateral variation of surface topography (m) at 0.010Myr (**A**), 50 Myr (**B**), (**C**) 100 Myr, and 200Myr (**D**). The topography reference value is −1 km.

fect of the two numerical simulations at 200 Myr, after the removal of the effect of a 1D-reference model calculated at the same time step (Fig. S1.13, Supplementary Material S1). The reference model was computed as the average density of all prisms having the same depths, at the time step 0.010 Myr and 200 Myr, respectively, to show the differences between the initial and final conditions. We can notice that the reference models of 1_Congo_weak1 and 2_Congo_weak2 show very small differences, with respect to the same time step. The reason is that the original different horizontal patterns of the two models are hidden by the computed average. On the other hand, the differences for the same model at the two time steps are relatively large at the crustal depths and more reduced below, according to the larger density variations occurring at the crustal levels during the extension.

Static Forward Gravity Model corrected for topography (SFGM tc): In order to separate the effects of the topography changes from those of density variations, induced by the mantle upwelling on the amplitude and trend of the static gravity anomalies, we implemented a static gravity model analogous to a Bouguer field of the two numerical simulations at 200 Myr, in which we suppressed the effects of the topography variations. To this aim, we removed from the computed gravity the signal produced by the first 23 km, which includes the effect of the sticky layer (first 20 km) and that of the surface topography variations, which are in a range of ± 3 km (Figs. 3 and 8). Afterwards, we subtracted a 1D-reference model, computed at the time step 200 Myr for each simulation and corrected for the topography effect to obtain a new gravity field, named SFGM_tc.

7. Forward gravity models results

The results of the DFGM show strong positive anomalies (80–300 mGal), related to the mass excess caused by the mantle upwelling, inducing density and topography variations (Fig. 16a-b). The amplitude of the anomalies is greater for the 2_Congo_weak2, as well as the features formed by their variations have a greater size. The highest and lowest values are localized in the uplifted and subsided areas (Figs. 3 and 8) and, as for the topography variations, form two elongated struc-

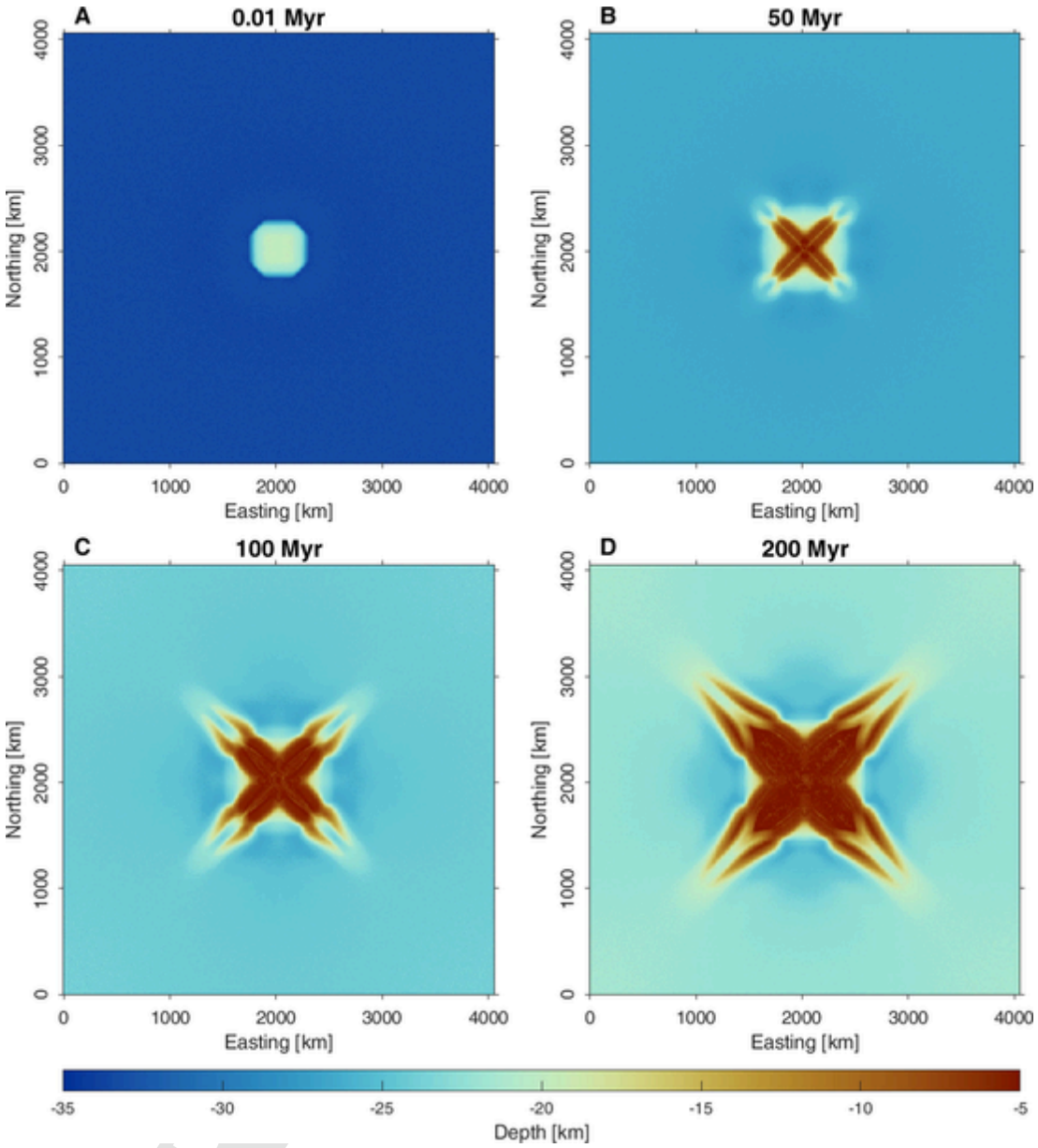

Fig. 9. Model 2_Congo_weak2. Lateral variation of the Moho topography (m), defined by the depth of the isodensity 3000 kg/m^3, at 0.010Myr (**A**), 50 Myr (**B**), 100 Myr (**C**), and 200Myr (**D**). The topography reference value is −35 km.

tures orthogonal each other. We can further notice that the applied multi-divergent velocity produces a change in the mass distribution not uniformly distributed, with a series of maxima and minima, affecting both the central and peripheral parts of the models.

Looking at the gravity anomalies along three cross-sections, we can observe in more detail the difference between the two models. In particular, the cross-sections A-B passing through one of the two elongated features of the 2_Congo_weak2 model evidences a minimum value in the central part (~250 mGal) surrounded by two maxima (~300 mGal). In contrast, the same cross-section of the 1_Congo_weak1 model shows a maximum in the centre (215 mGal), surrounded by other two secondary maxima (200 mGal). The different trend of anomalies indicates that the deformation simulated by 2_Congo_weak2 model reached a more mature rift stage, than that simulated by the first model. Indeed, the maximum in the centre observed in 1_Congo_weak1 model is the effect of the mantle upwelling localized in a narrower zone than in 2_Congo_weak2 model, as can be observed in the density-depth distribution (Figs. 14-15).

The cross-section C-D, 45° oriented with respect to the direction of the elongated orthogonal structures, shows that the positive anomaly (>250 mGal) in the centre of the model 1_Congo_weak1 forms a maximum (about 250 mGal) surrounded by two minima of about 100 mGal. In contrast, in the other model, we observe along the same cross-section an alternation of minima and maxima spanning in a smaller range (170–230 mGal). On the other hand, the trend of the gravity anomalies along the third cross-section, perpendicular to one of the elongated structures (E-F), is the same for both models, showing a minimum in the centre, surrounded by two maxima, which have a lower amplitude in the 1_Congo_weak1 model. Therefore, the two models considered produce similar anomalies variations in their peripheral parts, while the different geometry design and initial temperature conditions assumed significantly influence the evolution of the deformation in the centre, causing a different trend and amplitude of the gravity anomalies.

The results of the *SFGM* show positive and negative gravity anomalies localized in the uplifted and subsided areas (Fig. 17(a-b)), forming two elongated structures orthogonal each other (as already observed in

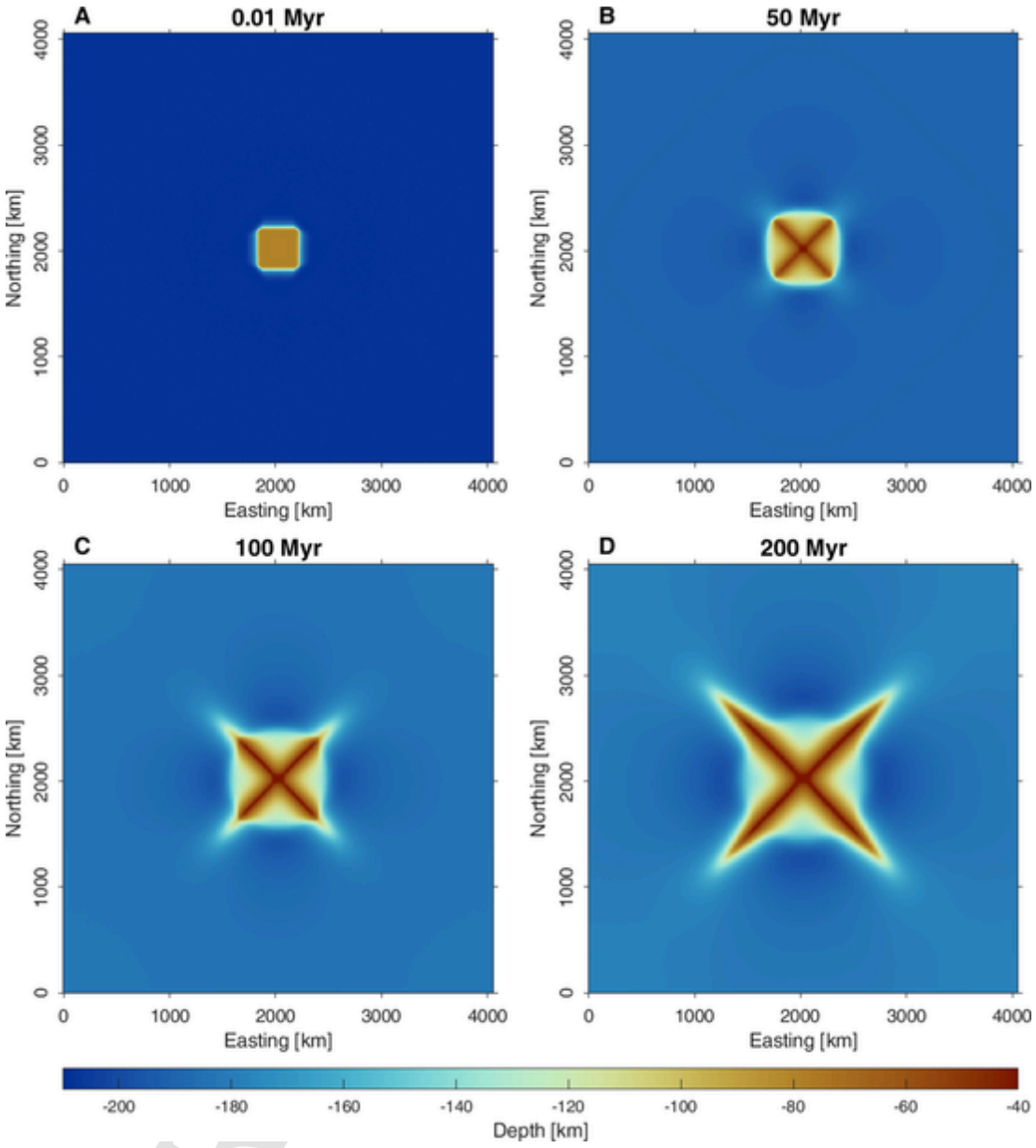

Fig. 10. Model 2_Congo_weak2. Lateral variation of topography (m) of the lithosphere-asthenosphere thermal boundary, defined as depth of the isotherm 1573 K (typical present-day reference value), at 0.010Myr (**A**), 50 Myr (**B**), 100 Myr (**C**), and 200Myr (**D**). The topography reference value is −210 km.

the *DFGM*). In general, the SFGM produces structures similar to those obtained from the DFGM. As before, 2_Congo_weak2 model causes anomalies of higher amplitude, distributed on a larger area, with respect to those of the 1_Congo_weak1 model. This can be ascribed to the different geometry design and initial temperature conditions assumed that, in case of 2_Congo_weak2 model, increase the speed of the extensional deformation simulated and enhance the mantle upwelling on a larger area.

The two models show also similar anomalies variation, with weak positive values (< 50 mGal) in the central area and along two elongated zones orthogonal each other, characterized by the uprising of the asthenosphere in correspondence of the strong subsidence of the surface topography (Fig. 3D and 8D). These structures are surrounded by zones of strong negative anomalies (-30 mGal to −90 mGal), which are in turn surrounded by zones of strong positive anomalies (70–130 mGal), corresponding to the areas of subsidence and uplift of the surface topography, respectively (Fig. 3D and 8D). These anomalies, reflecting the formation of zones of mass excess and defect, with respect the 1D reference model, can be explained by the combined effect of the lateral variations of surface topography and temperature of the upwelling mantle that decreases moving away from the center. To this purpose, we should notice that the uplift of the surface topography is induced by the propagation of the extensional deformation from the central weak zone towards the more rigid cratonic areas and thus it is not accompanied by a crustal thickening.

The results of the *SFGM* are also comparable with the gravity disturbance displayed in Maddaloni et al. (2021), considering that the observed field reflects also the effect of sediments, not considered in the numerical models. With this aim, we compared the values of the models along three cross-sections with that of the gravity disturbance obtained along several cross-sections (Fig. 18). Since the numerical models cannot reproduce all the small heterogeneities of the structures formed during the evolution of the *CB*, the *SFGM* produces a smoother signal with higher amplitude, compared to that of the gravity disturbance. On the other hand, the observed gravity field is characterized by the alternation of weak positive and strong negative anomalies, with a trend

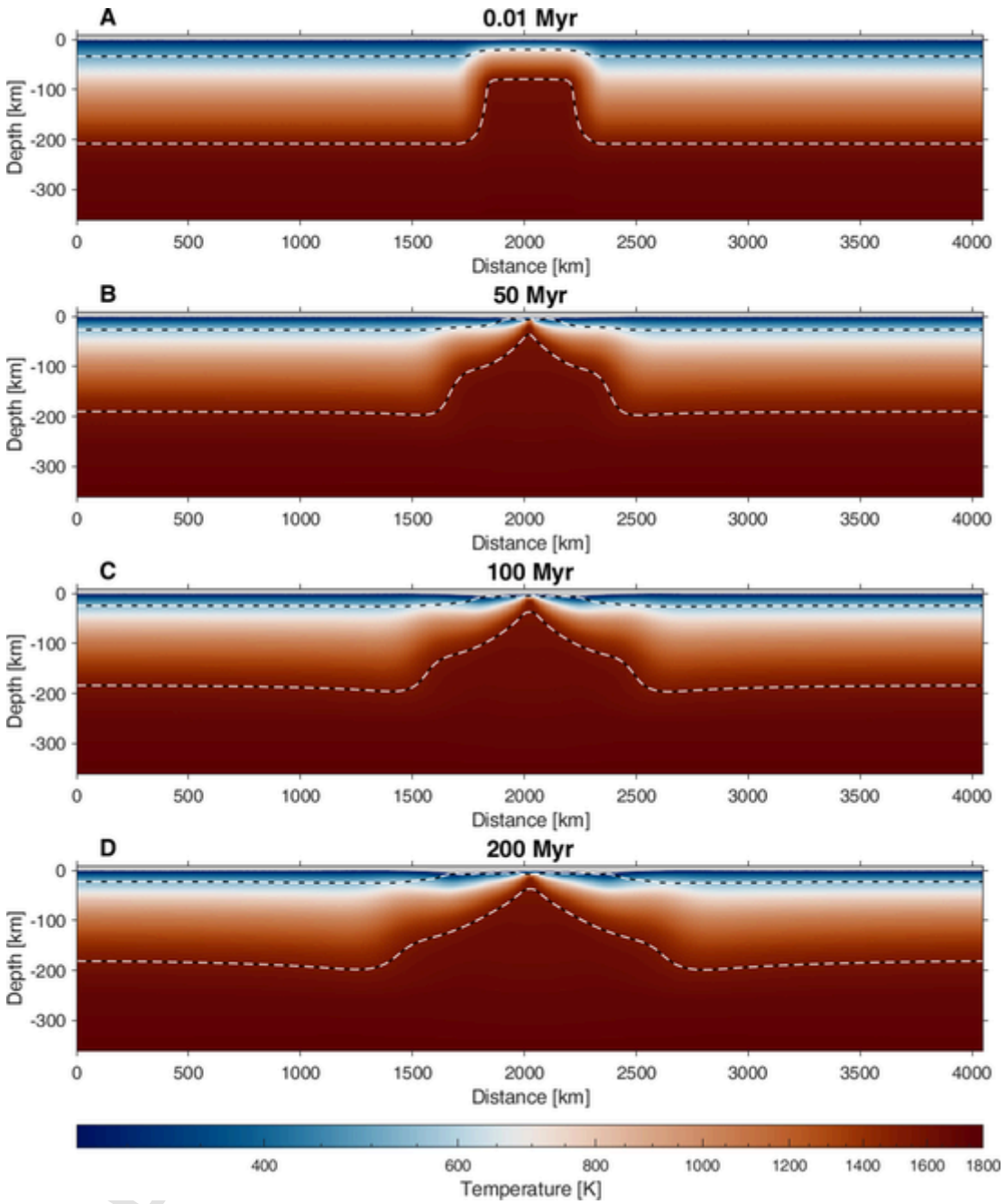

Fig. 11. Model 2_Congo_weak2. Depth-temperature (K) variation, along a N—S cross-section through the model centre displayed in Fig. 14, at 0.010 Myr (**A**), 50 Myr (**B**), 100 Myr (**C**), and 200Myr (**D**). Black-white dashed lines show the Moho depth, defined as the depth of the isodensity 3000 kg/m^3, and the depth of the lithosphere and asthenosphere boundary (LAB), defined as depth of the isotherm 1573 K (typical present-day reference value). Vertical scale is increased by 100 % with respect to the horizontal axis.

similar to that of the *SFGM* along the three cross-sections. For instance, the trend of the cross-section A-B and C-D of the model 1_Congo_weak1 resembles that displayed by the cross-sections AA' and EE' of the observed gravity field (Fig. 18).

In the same way, the trend of the cross-section C-D of the 2_Congo_weak2 model resembles that of the cross-sections BB' and DD' of the gravity disturbance (Fig. 18). However, the observed gravity anomalies are prevalently related to the density variations in the crust, since the topography of the area is quite low (< 300 m, Fig. 13). In particular, the minimum values are located in correspondence of the deep sedimentary basins and thus are likely induced by the low density of the sediments. In contrast, the positive values fall in correspondence of the tectonic highs (e.g., Kiri High, Mossaka High), likely characterized by a high-density crystalline crust (Maddaloni et al., 2021). There are also some parts of the *CB*, in which the density of the different crustal layers produces small gravity anomalies (between −25 mGal and 10 mGal), as along cross-section C—C' (Fig. 18). This trend is similar to that of the cross-section A-B of the 2_Congo_weak2, which instead reflects the combined effect of the topography subsidence and density increase, due to the asthenospheric uprising (Fig. 18).

On the other hand, the *SFGM_tc* model enhances the effect of the anomalous mass below the surface topography (–23 km). In particular, we should notice the strong increase of the positive anomalies (up to 200 mGal) in the central part of the model, which are more affected by the mantle upwelling. In contrast, the edges of the two elongated structures show weak anomalies (± 20 mGal), indicating that the effect of

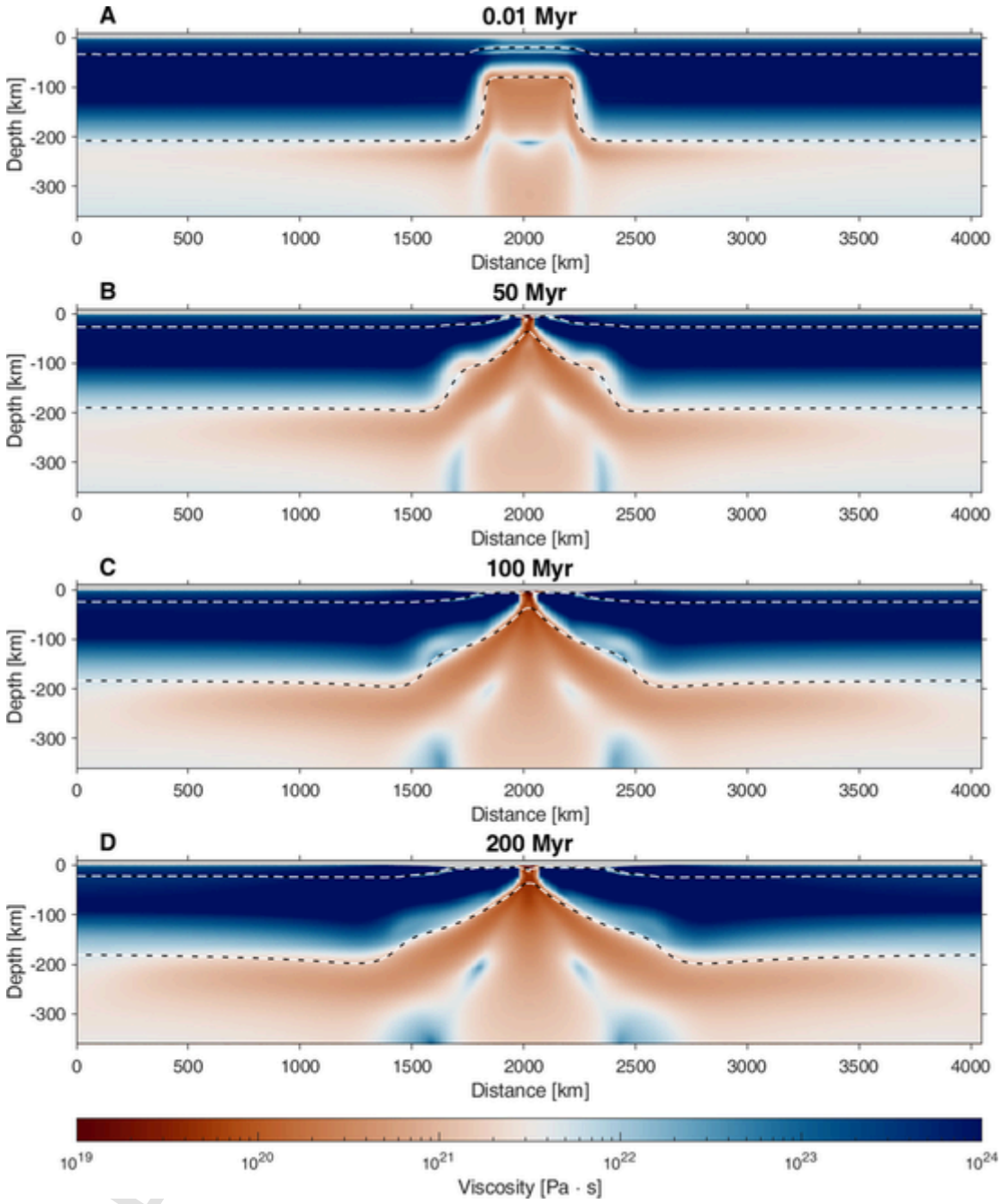

Fig. 12. Model 2_ Congo_weak2. Depth-viscosity variation (Pa s) along a N—S cross-section through the model centre displayed in Fig. 14, at 0.010Myr (**A**), 50 Myr (**B**), 100 Myr (**C**), and 200 Myr (**D**). Black-white dashed lines show the Moho depth, defined as the depth of the isodensity 3000 kg/m^3, and the depth of the lithosphere and asthenosphere boundary (LAB), defined as depth of the isotherm 1573 K (typical present-day reference value). Vertical scale is increased by 100 % with respect to the horizontal axis.

the anomalous mass below –23 km depth is negligible. In order to distinguish the effects of the topography and density variation in the static model of the gravity field, we derived three cross-sections of the *SFGM* and *SFGM_tc* model (Figs. 17 and 19). The first cross-sections A-B of the SFGM_tc model (Fig. 17B and 19B) evidences in both simulations a broad area of positive values (>150 mGal), with the centre characterized by a maximum in model 1_Congo_weak1 and a relative minimum in model 2_Congo_weak2. These differences are related to the variations of the asthenospheric flow occurring during the tectonic extension in the two models. In the second model (2_Congo_weak2), the asthenospheric uprising affects a larger area, producing an excess of mass along two orthogonal directions (Fig. 19A). The gravity anomalies along the cross-section C-D, 45° oriented with respect to the direction of the elongated orthogonal structures, have similar shape and amplitude in both models with a large positive anomaly (~180 mGal) and a minimum in the center (~150 mGal). The gravity anomalies along the third cross-section, perpendicular to one of the elongated orthogonal structure (E-F), show also very similar trends and amplitudes in the two models (Fig. 17B and 19B). We can notice that along both cross-sections A-B and C-D, the *SFGM_tc* produces anomalies of much larger amplitudes than those of the SFGM (Figs. 17 and 19). Indeed, in the last forward model, the effect of the topography variation (i.e. the formation of a large topography depression) almost counteracts that of the density increase due to the asthenospheric upwelling. On the other hand, along the cross-sections E-F (1_Congo_weak1 model) and G-H (2_Congo_weak2 model), the *SFGM_tc* shows quite weak positive anomalies (<50 mGal),

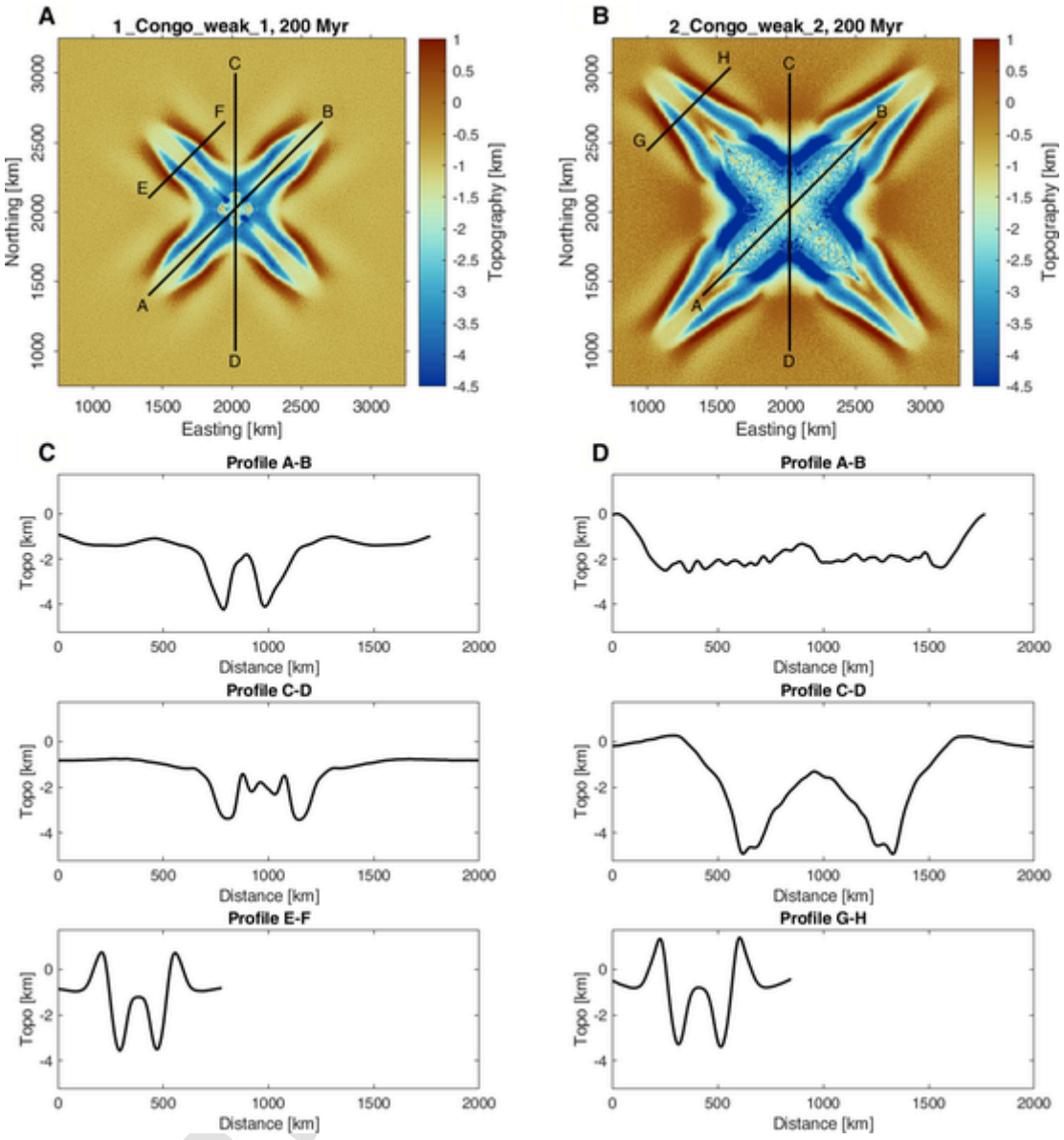

Fig. 13. Surface topography variation at 200 Myr of the 1_Congo_weak1 and 2_Congo_weak2 model. (**A-B**) Lateral surface topography variations. Black lines with labels show the location of three chosen cross-sections. (**C-D**) Lateral topography variations along three cross-sections displayed in A and B.

compared to the large range (±100 mGal) of the *SFGM*. This indicates that in the last case, the effect of the sharp topography variations is much more significant than that of the density changes.

8. Discussion

Tectonic reconstructions before the *CB* initiation (about 1100 Myr, Delvaux et al., 2021) are quite uncertain, due to the very limited and sparse geological data. However, the large number of continental collisions dated between 2100 and 1800 Myr records the formation of the Earth's oldest known supercontinent, named Columbia supercontinent, assembled between 2000 and 1600 Myr (Goldberg, 2010). Based on magmatism, paleomagnetism, and dike swarms, previous studies dated the initial phase of break-up of this supercontinent just after its maximum packing (1900–1700 Myr), while the final break-up probably occurred between 1300 and 1200 Myr (e.g., Nance et al., 2013 and references therein). In this tectonic scenario, the *CB* formation can be related to one of the final phases of the Columbia break-up, resulted in several-failed rift (e.g., Goldberg, 2010).

At this time, the cratonic blocks, being already dispersed after the fragmentation of Columbia could have been more likely subjected to a multi-extensional stress, responsible for the *CB* formation. To support this hypothesis, we have to refer to the thermo-compositional structure of the underlying *CB* lithosphere, which is apparently similar to those of other old cratonic areas, characterized by thick cold roots (e.g., Sebai et al., 2006; Pasyanos and Nyblade, 2007; Begg et al., 2009; Fishwick, 2010; Emry et al., 2019; Celli et al., 2020). In particular, the recent seismic tomography model of Emry et al. (2019) and Celli et al. (2020) have shown that the Congo Craton is composed of at least three cratonic blocks, 200–250 km thick, with eroded margins. Furthermore, the lithospheric thermal structure, reflected by the surface heat flow values (Lucazeau et al., 2015) and obtained from inversion of this seismic tomography model, taking into account the mantle compositional variations (Finger et al., 2022), indicate typical cratonic temperatures. On the other hand, mantle density variations, induced by the composition, show small depletion in *Fe* components, which is expressed by the Mg

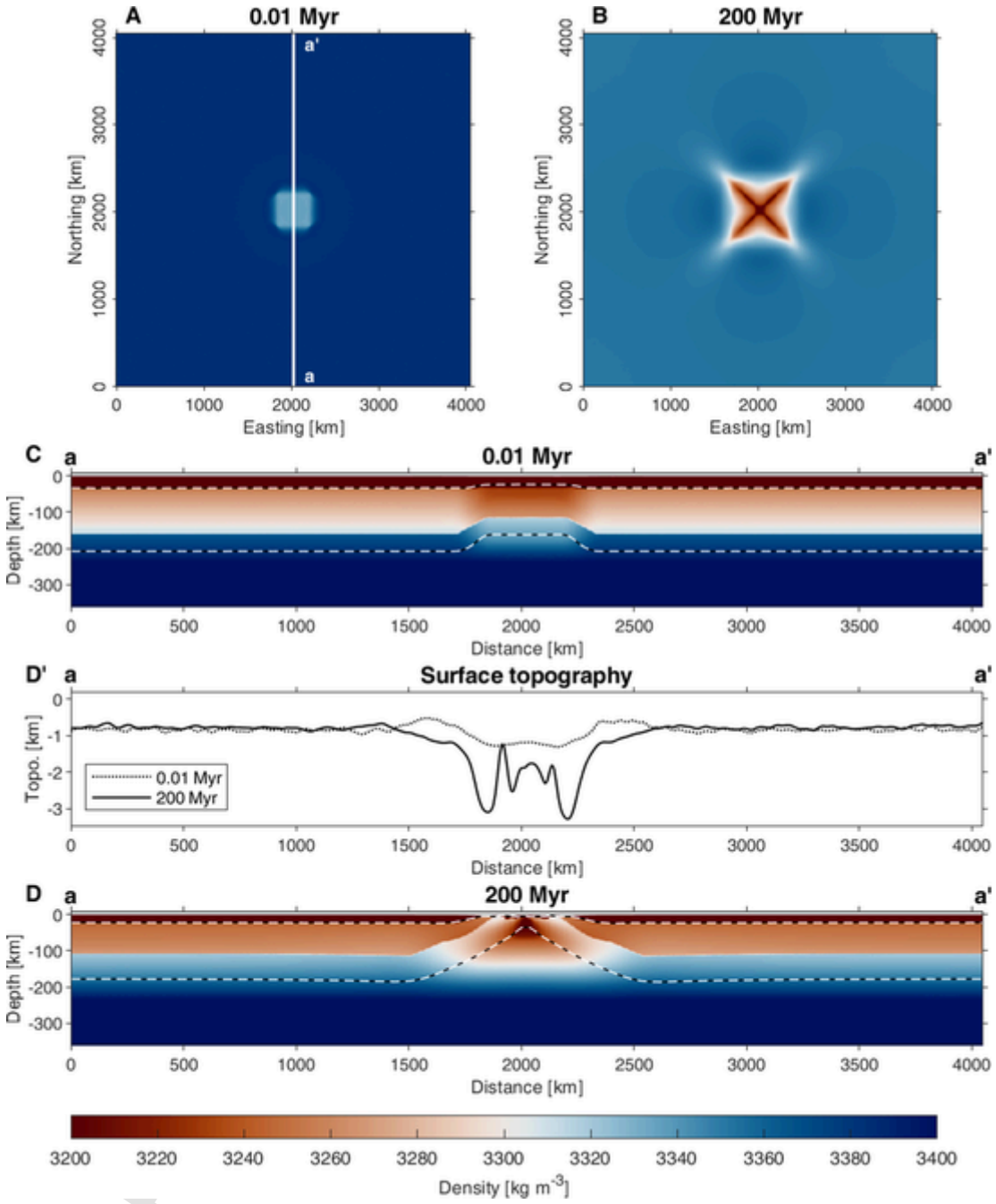

Fig. 14. Model 1_Congo_weak1. Lateral variation of density (kg/m^3) at the base of the lithosphere, defined as depth of the isotherm 1573 K (typical present-day reference value), at 0.010Myr (**A**), and 200 Myr (**B**). Depth-density (kg/m^3) variation, along a N—S cross-section displayed in A, at 0.010Myr (**C**), and 200 Myr (**D**), with lateral variation of surface topography (**D'**). Black-white dashed lines show the Moho depth, defined as the depth of the isodensity 3000 kg/m^3, and the depth of the lithosphere and asthenosphere boundary (LAB), defined as depth of the isotherm 1573 K (typical present-day reference value). Vertical scale increased by 100 % with respect to the horizontal axis.

number ([1]Mg # < 91) (Finger et al., 2022). This means that the original lithosphere of the Archean cratons composing the Congo Craton, could have been destroyed and regrown or simply rejuvenated. This event likely occurred during the rift phase that determined the *CB* formation. A rifting phase can be the effect of a mantle plume action under different types of regional tectonic stress (Foley and O'Neill, 2021; Liu t al., 2021). In case of regional extensional forces, the cratons can undergo rifting and thus thin their lithosphere, while compressional tectonic forces would prevent the destructive action of a plume. In case of compressional stress, the plume, exerting local extension, can induce an initial rift phase, only with minor thinning of the cratonic roots. In this scenario, plume melts could not reach the surface, but only metasomatize the upper mantle and possibly accretionate at the base of the crust/mantle lithosphere. This process would also favour the regrowth of the cratonic roots after the local thinning, due to the plume action, and enhance the topographic subsidence. If this would have been the case of the *CB*, the compressional stress could have been the effect of the ridge push of mid-oceanic rifts, opened during the last pulse of breakup of Columbia, occurred between 1600 and 1200 Myr or related to the following Rodinia assembly (Nance et al., 2013 and references therein).

[1] Mg# $= 100 \times Mg/(Mg + Fe)$.

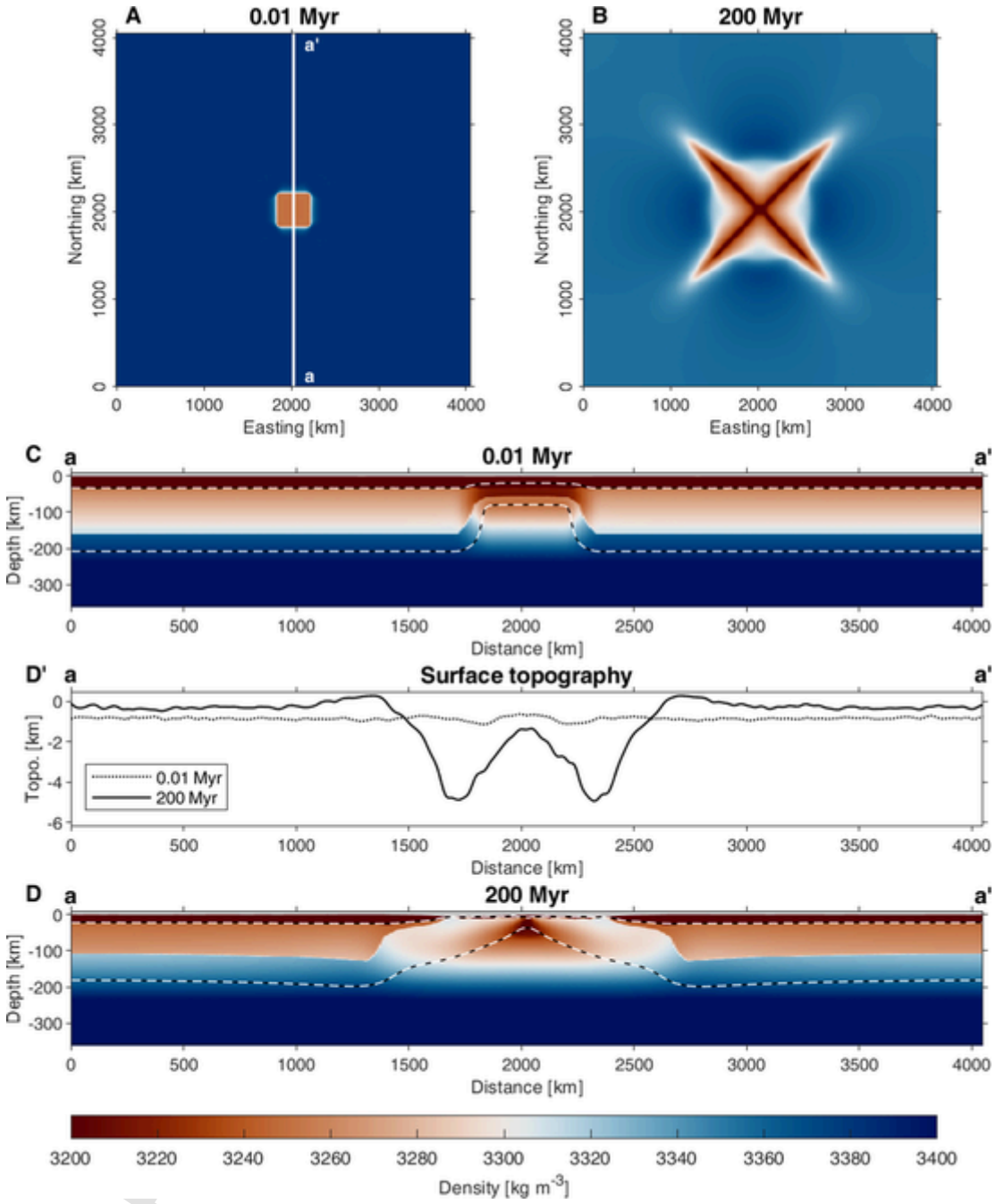

Fig. 15. Model 2_Congo_weak2. Lateral variation of density (kg/m^3) at the lithosphere-asthenosphere thermal boundary, defined as depth of the isotherm 1573 K (typical present-day reference value), at 0.010Myr (**A**), and 200 Myr (**B**). Depth-density (kg/m^3) variation, along a N—S cross-section displayed in A, at 0.010Myr (**C**), and 200 Myr (**D**), with lateral variation of surface topography (**D'**). Black-white dashed lines show the Moho depth, defined as the depth of the isodensity 3000 kg/m^3, and the depth of the lithosphere and asthenosphere boundary (LAB), defined as depth of the isotherm 1573 K (typical present-day reference value). Vertical scale is increased by 100 % with respect to the horizontal axis.

The hypothesis of the interplay of regional compressional stress field with mantle plume is appealing, since it fits the geophysical observations. In particular, it would justify (1) the presence of a crust thicker (about 40 km, Ojo et al., 2022) than it would be in case of isostatic equilibrium; (2) the small *Fe*-components depletion of the lithosphere underlying the *CB* (Finger et al., 2022). In addition, the removal of the lithospheric roots due to the plumes' action and their subsequent restoration has been proposed for both the South American and African cratons by Hu et al. (2018). However, we rule out this hypothesis, due to the absence of a large igneous province of Mesoproterozoic age in the study area and surroundings. Furthermore, no short-scale lateral mantle velocity variations have been detected from seismic tomography within the cratonic blocks composing the Congo Craton, which would mark episodes of thinning and rethickening of the lithosphere (Liu et al., 2021). In contrast, we can speculate that slow multi-divergent velocity, acting on a cratonic lithosphere, could have induced the initial subsidence of the *CB* in a weaker part of the craton. Such a weak zone could have represented the suture between the different cratonic pieces (de Wit and Linol, 2015) or have simply been an inherited heterogeneity from the processes of the cratons formation.

The relatively deep crustal and lithospheric roots indicate that the extensional stress that initiated the *CB* subsidence has not induced sig-

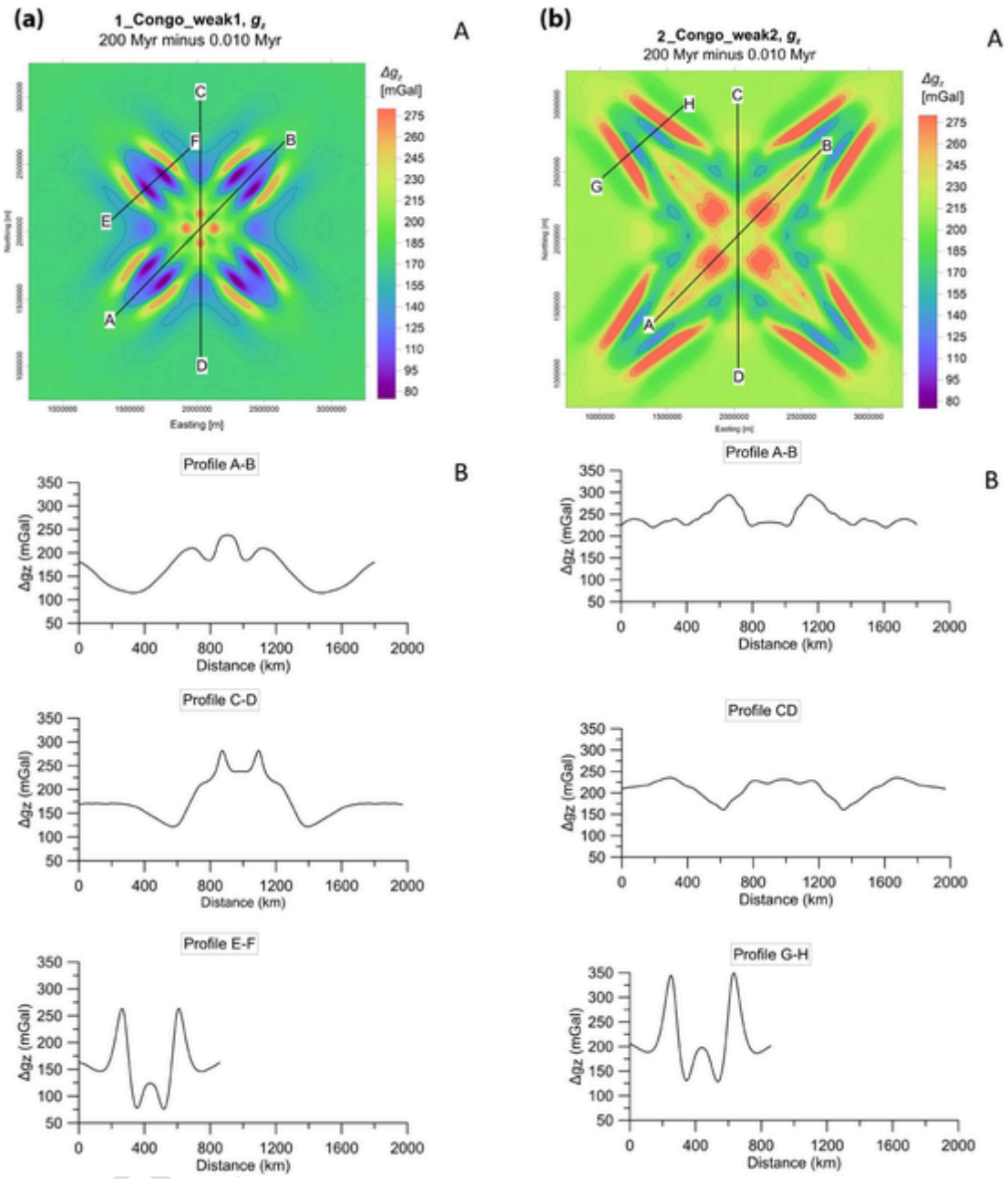

Fig. 16. Dynamic forward gravity modelling (DFGM) of the **(a)** 1_Congo_weak1 and **(b)** 2_Congo_weak2 model. (**A**) Horizontal plane visualization of the gravity anomalies. Black lines with labels show the location of three chosen cross-sections; (**B**) Lateral gravity variations along three cross-sections displayed in A.

nificant crustal/lithospheric thinning, possibly, because it did not act for a sufficient time, being followed, after about 100 Myr, by compressional stress related to the Rodinia assembly. The presence of some small mafic bodies at crustal depths, as a product of the lithospheric extension, is supported by the gravity models performed in Maddaloni et al. (2021). However, the shear wave velocities are not very high in the lowermost part of the crust to hypothesize thick magmatic underplating at the base of the crust (Ojo et al., 2022). Therefore, we suppose that the injection of mafic bodies would have occurred only sporadically and that most of the crust would have been preserved. We can also speculate that the asthenospheric upwelling, induced by the extensional stress, has metasomatized the lithospheric cratonic roots, producing weakening and densification of the original cratonic lithosphere. This process that probably caused a small erosion of the lithospheric roots, but left almost intact the crustal thickness, could have enhanced the basin subsidence initiated by the action of extensional stress. The eroded lithosphere could have been replaced by the cooled asthenosphere, during the post-rift phase, lasting 300 Myr. During this period, there are no signs of tectonic stress related to the Rodinia assembly and break-up.

The initial rift phase produced stronger subsidence in the northern part of the *CB*, as observed by the greater thickness of the *syn*-rift sediments located in that part of the basin. On the other hand, the following compressional stress, related to the Gondwana assembly, enhanced the initial subsidence related to the rift extension, in the southern part, forming the deepest depocenters of the *CB* (Delvaux et al., 2021). Therefore, both the extensional and compressional phases might not have acted uniformly on the Cuvette Centrale, but along different preferential directions. The succession of compressional events to a rift extension occurred also in other *ICBs*, such as those of North America, (e.g., Klein and Hsui, 1987) and Australia, where the phases of intracontinental orogeny lead to the separation of the Centralian Superbasin

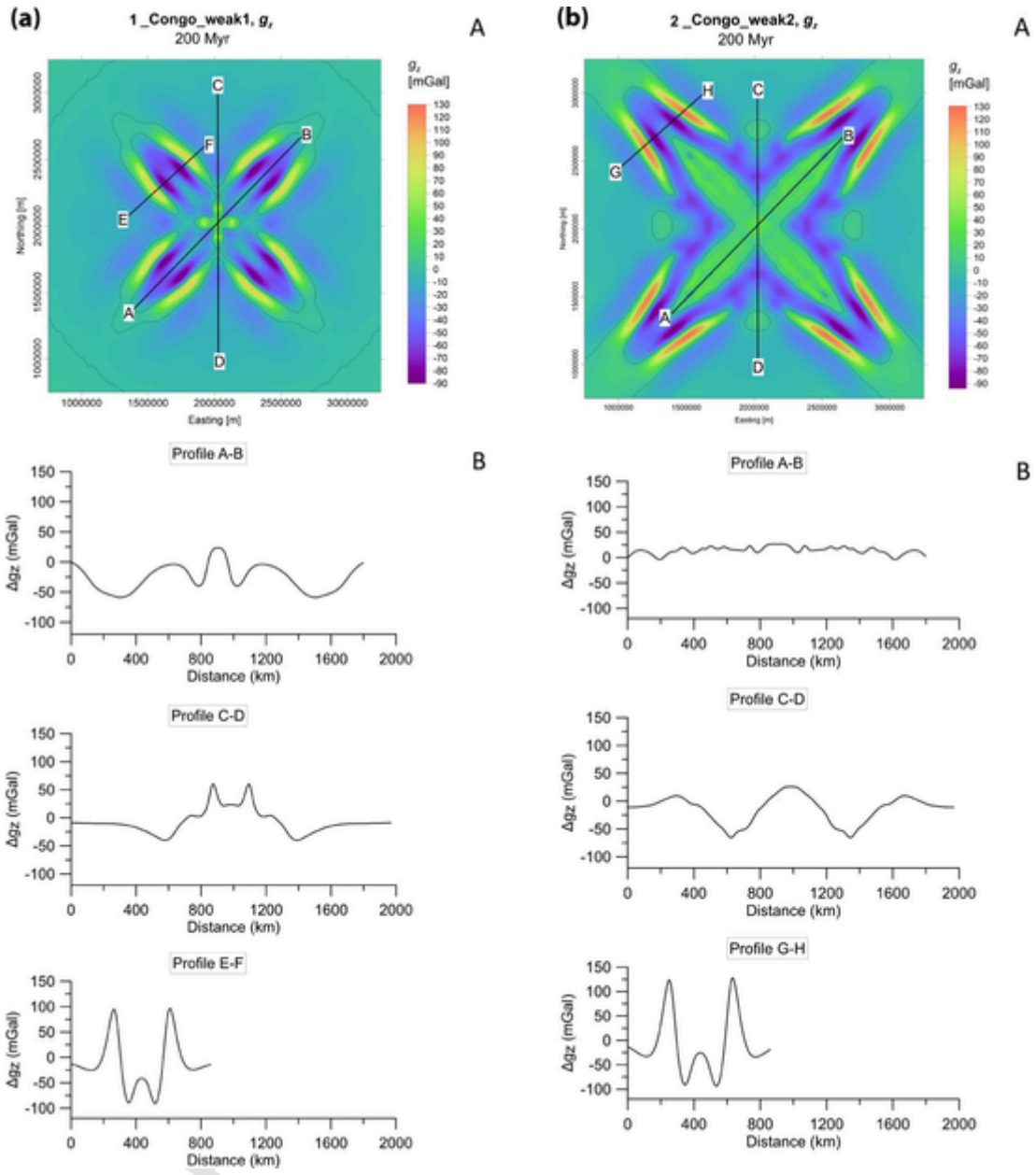

Fig. 17. Static forward gravity modelling (SFGM) of the **(a)** 1_Congo_weak1 and **(b)** 2_Congo_weak2 model. (**A**) Horizontal plane visualization of the gravity anomalies. Black lines with labels show the location of three chosen cross-sections. (**B**) Lateral variations of the gravity anomalies along three cross-sections displayed in A.

of Australia in four main basins (Officer, Amadeus, Ngalia and Georgina basins), between 600 and 300 Myr (e.g., Lindsay, 2002). It has been demonstrated that small variations of the far field stresses cause period of subsidence acceleration, deceleration and even inversion (Perron et al., 2020). Therefore, periodic changes in far field tectonic can significantly complicate the tectono-stratigraphic architecture of the basins, by introducing stratigraphic unconformities between different neighboring basins. In the *CB*, two main episodes of far field compression gave origin to the major tectonic unconformities (Pan-African and Basal Jurassic), which produced a first-order subdivision of the sedimentary sequences in three age groups, but did not modify the main rift structures (Delvaux et al., 2021).

Therefore, considering that the formation of the first-order heterogeneities of the basement depth of the *CB* have been induced by an extensional stress (Delvaux et al., 2021), we implemented 3D numerical models applying a uniform multi-divergent velocity to a cratonic lithosphere. The recent study of Gerya and Burov (2018) tested the hypothesis that the multi-divergent velocity applied to an oceanic lithosphere could have been responsible for the formation of triple junctions from the evolution of the transient quadruple junctions. They in particular found that a quadruple *rift-rift-rift-rift* junction is a characteristic lithospheric breakup structure in case of a single thermal/rheological perturbation, whereas multiple triple *rift-rift-rift* junctions develop from more complex perturbation patterns (Gerya and Burov, 2018) and/or due to influence of a mantle plume (Koptev et al., 2018). In our case, we first observe the formation of a circular central depression with uplifted edges, which then gradually evolves into a quadruple *rift-rift-rift-rift* junction. This is also a typical effect of previous bi-directional oceanic extension models with single central thermal/rheological perturbation (Gerya and Burov, 2018). On the other hand, in our models, the resulting surface topography within the circular-depressed area is rather complex and characterized by a series of topographic lows and highs aligned along a preferential direction. The symmetry of the formed structures is due to the assumed geometry design and low extensional

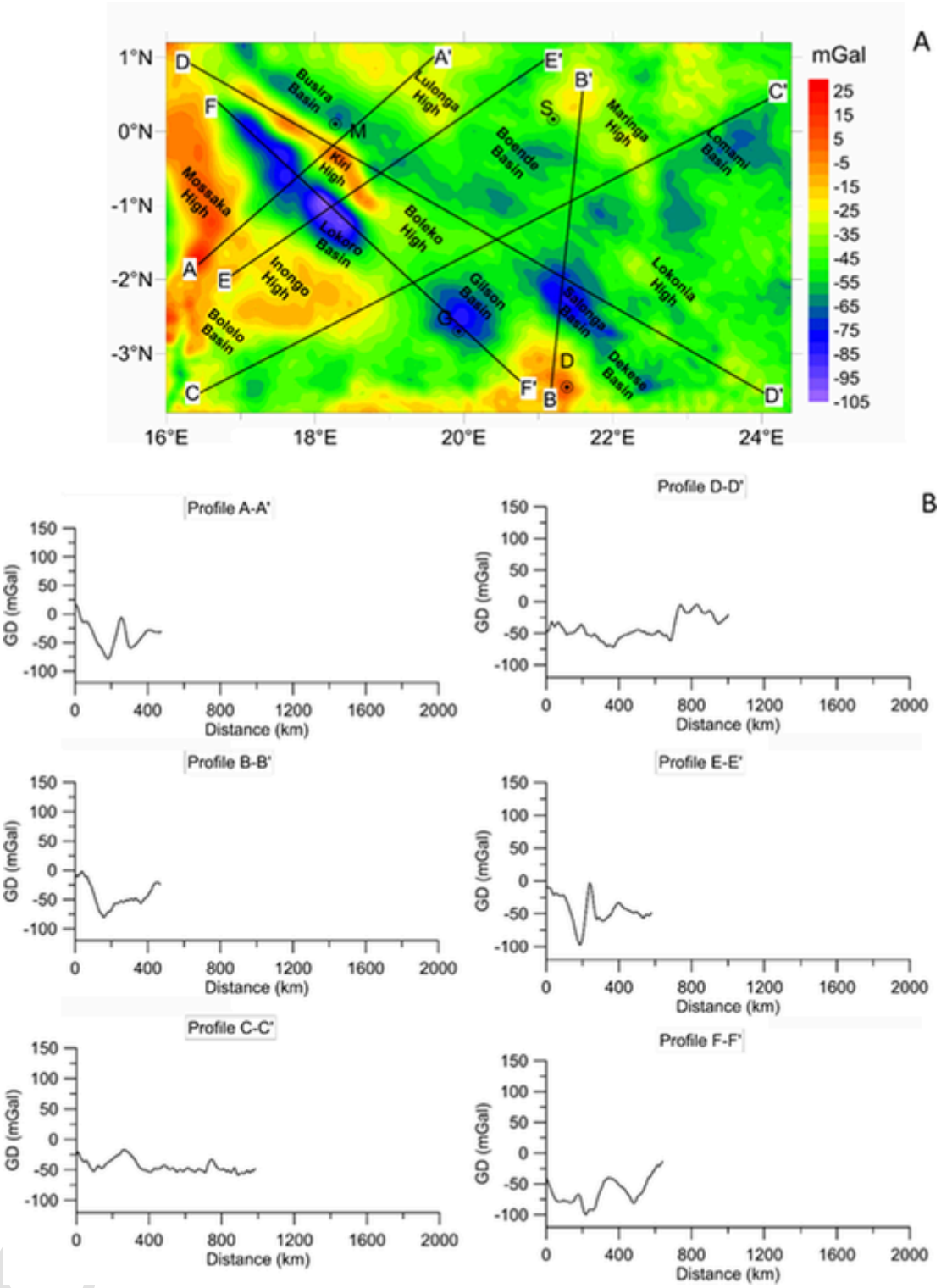

Fig. 18. Gravity disturbance of the *CB* (modified after Maddaloni et al., 2021). (**A**) Map of the gravity disturbance. Black lines with labels show the location of six chosen cross-sections; (**B**) Lateral variation of the gravity disturbance along six cross-sections displayed in A.

rate applied. The last one determines also the absence of magmatic products during the rift structures formation. Furthermore, we noticed that the maximum subsidence during the first 50–100 Myr is concentrated along two elongated structures orthogonal each other that form a quadruple junction. This feature does not evolve in a triple junction as in the numerical models of Gerya and Burov (2018), probably because of the low velocity rate assumed in our models. On the other hand, interconnected rifts forming triple junctions are the direct effect of the combination of symmetric and asymmetric divergent velocities applied (Koptev et al., 2018).

The elongated structures are the direct effect of the asthenospheric upwelling, which replaces the less dense mantle lithosphere and later (after ~ 100 Myr) the crust. However, when the asthenosphere rises close to the surface topography, the last one tends to uplift. Since the crust is currently quite thick (Ojo et al., 2022), the results at the last time step (200 Myr) are the product of an advanced stage of deforma-

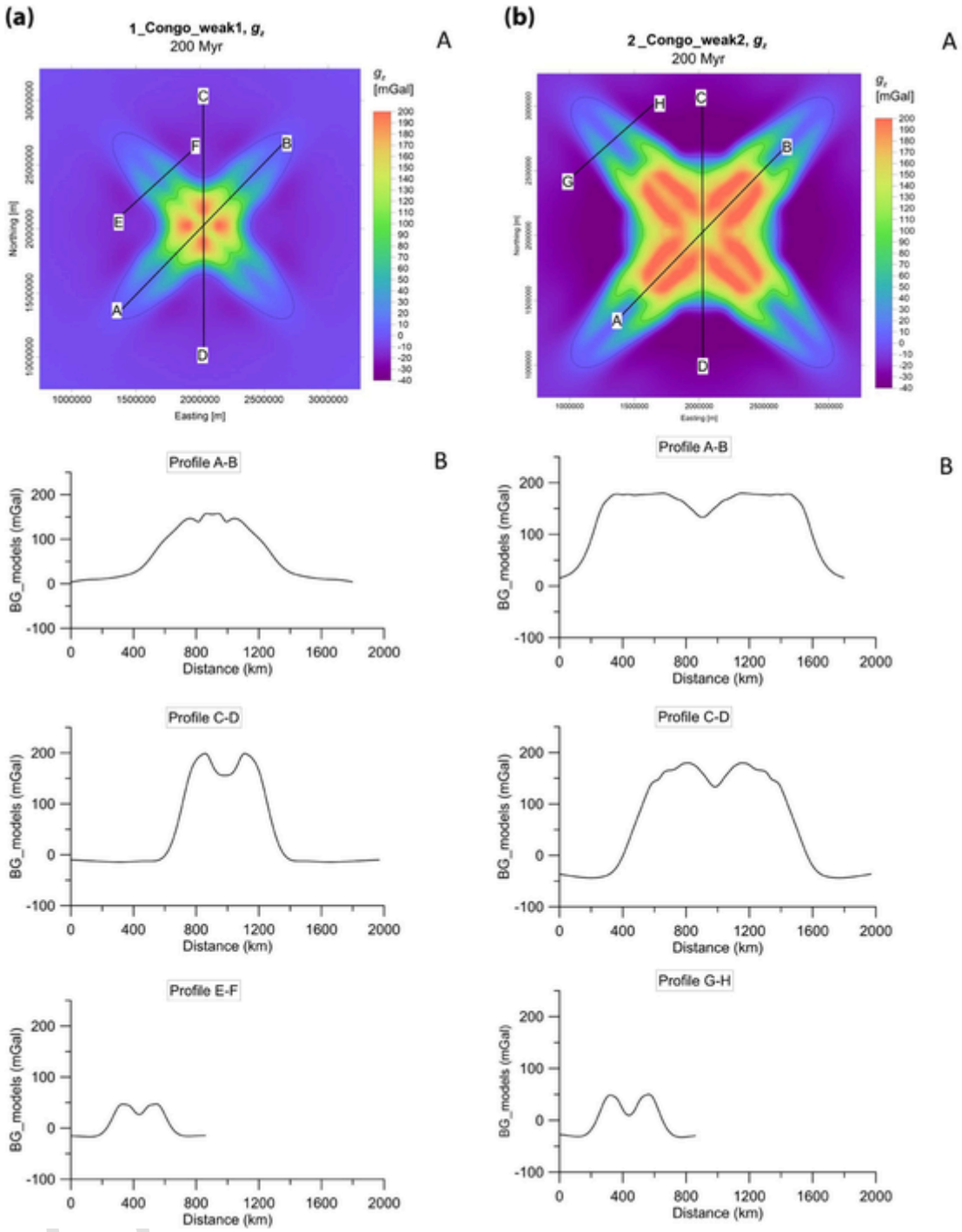

Fig. 19. Static forward gravity modelling corrected for topography (SFGM_tc) of the **(a)** 1_Congo_weak1 and **(b)** 2_Congo_weak2 model. (**A**) Horizontal plane visualization of the gravity anomalies. Black lines with labels show the location of three chosen cross-sections; (**B**) Lateral gravity anomalies variation along three cross-sections displayed in A.

tion in which the original crust has been mostly destroyed. This stage, very likely, was not reached by the *CB* during the rift phase. However, we performed the numerical models until this time step, both to take into account the maximum possible duration of the rift phase and demonstrate the long-term stability of the structures formed. To this purpose, we should consider that the time of their appearance varies for each numerical test, depending on the initial model set-up (section 3 and 4). This makes more difficult the comparison between the modelled and reconstructed present-day basement depth. In addition, we should consider that the *CB* basement depth reflects also the effects of the following tectonic compressional phases and of sedimentation/erosion, which are processes not simulated in this study. We do also not know if the divergent velocity acted uniformly on the Congo craton or more significantly along one direction. However, despite all the assumptions used in the numerical models, the resulting topography heterogeneities resemble those of the current basement depth. In particular, our models could reproduce the sharp topography variations (2–3 km) within a short distance (about 100 km), which characterize the basement depth of the *CB*, for instance, at the transition between the Dekese basin and Lokonia High (Delvaux et al., 2021; Maddaloni et al., 2021). We could further notice that the effects of the multi-extensional stress propagate also in the peripheral parts of the central weak zone, which become

progressively uplifted. These features resemble the mobile belts located around the edges of the *CB*.

The comparison of the modelled static gravity fields with the gravity disturbance anomalies shows that the former produces a smoother signal with higher amplitude, compared to the latter. In particular, the modelled fields, depending on the topography and density variations, induced by the mantle upwelling, could reproduce a trend of anomalies similar to that observed, but not the shape of all the small anomalies related to the sediments distribution and local heterogeneities of the basement, present already before the *syn*-rift phase or acquired during the following tectonic events. The basement heterogeneity can have played a significant role on the long-term subsidence of the *ICBs*, by resisting local isostatic re-equilibration (Perron et al., 2020) and thus should be included in the future numerical models to reproduce the short wavelength of the basement depth variations.

As stated before, the subsidence of the *CB* continued during the post rift-phase and have increased the depth of the depocenters formed during the *syn*-rift phase, but not modified the main structures of the basin. Indeed, as demonstrated in the study of Armitage and Allen (2012), the low-strain rates, at which the extensional deformation of the basins lying on a thick cratonic lithosphere occurs, produces a post-rift phase, characterized by a long-subsidence decay that is typical of the *ICBs*. The sedimentation has the effect to further increase the duration of the post-rift subsidence, as demonstrated by the 3D models of Cacace and Scheck-Wenderoth (2016), which simulate basin subsidence by imposing a thermal anomaly in the deep lithosphere. Their results show that the sediments deposition, reducing the heating loss ('blanketing effect'), significantly slows the post-rift subsidence and at the same time favors decoupling of the crust from the mantle lithosphere, causing a more distributed deformation. These effects of sedimentation on the basement depth variations can be investigated in the near future in the *CB*, as well as in any other *ICB* that originated from a rift phase, by implementing numerical models, keeping similar kinematic boundaries and geometry designs used in this study.

Other previous studies (e.g., Downey and Gurnis, 2009; Crosby et al., 2010; Buiter et al., 2012) have interpreted seismic tomography models, basin data analyses, and satellite gravity data of the *CB*, to investigate the origin of the huge negative free-air and geoid gravity anomalies characterizing the basin. In particular, they linked these anomalies to the effect of sediments (Buiter et al., 2012) or mantle structure and its dynamics (Downey and Gurnis, 2009; Crosby et al., 2010). In particular, Downey and Gurnis (2009) linked the *CB* formation and the negative gravity anomalies to a downward dynamic force exerted by a high-density body located in the lithosphere. However, the recent thermo-compositional model of Finger et al (2022) does not evidence the presence of high-density bodies in the mantle lithosphere of the *CB*.

The long- term evolution of the *CB*, as well as of other *ICBs*, have been influenced by other climatic and tectonic events, which caused the migration of the depocenters formed during the *syn*-rift phases. Perron et al. (2018), using satellite images, geological, and potential field data to investigate the basement structure of the basins lying on the African metacraton (Reggane, Ahnet, Mouydir and Illizi basins) discovered that these basins and the *CB* are coeval and have been affected by the compression of the Pan African collision that lead to the Gondwana assembly). The effect of these other processes on the *CB* basement can be tested through numerical models, starting from the results obtained in this study and using the reconstructed stratigraphy and analysis of well-log data previously achieved (Delvaux et al., 2021).

Furthermore, we should consider that the long-term evolution of the *ICBs* can be often influenced by a long-lasting negative dynamic topography, induced by the deep lithospheric cratonic roots (Heine et al., 2008) and in response to the onset of upwelling plumes in the neighboring areas (Crosby et al., 2010). Therefore, in the near future, it could be interesting to analyze the dynamic topography of the *CB*, using seismic tomography models and geoid anomalies, in order to improve the plate kinematic frameworks of the central African continent. The computation from 3D numerical models of time-dependent surface topography, induced by the mantle upwelling occurred during the first phase of the *CB* formation, will help quantify the initial dynamic topography.

9. Conclusions and outlooks

In this study, we implemented 3D numerical models, using I3ELVIS numerical code, to validate the hypothesis that a multi-divergent velocity, acting on a cratonic area, caused rift systems formation responsible for the first order heterogeneities of the basement depth of the Congo basin (*CB*). The numerical models were implemented, considering that the assembly of the cratons composing the Congo Craton could have left a weak 'suture' zone in the centre, representing the central part of the *CB*. Furthermore, we applied a multi-divergent uniform velocity of 2.5 mm/yr for each side of the model, for a maximum time lapse of 200 Myr.

- The main results, in terms of topography variations, given by the reference models, 1_Congo_weak1 and 2_Congo_weak2, distinct for the geometry design and initial temperature conditions applied to the weak zone, well reproduce the first-order basement depth variations of the *CB*. In particular, they produce the formation of an almost circular depressed area in the central part of the model, intersected by two strongly subsided elongated structures, orthogonal each other, whose topography tends to raise with time.
- Assuming a larger size of the weak zone (20 % of the entire model) in 2_Congo_weak2 model increases the speed of the deformation and size of the structures, which form in an earlier time step than when the weak zone is reduced to the half in 1_Congo_weak1 model. Oher models implemented produce results similar to those of the reference models or inconsistent with the actual basement depth variations of the *CB*.
- The consistency of the results of the two reference numerical models was checked by implementing their dynamic and static forward gravity models (*DFGM* and *SFGM*, respectively). The results of the *DFGM*, consist in positive anomalies induced by the mass excess produced by the asthenospheric upwelling and their lateral changes depend on the topography variations (strong and weak positive anomalies correspond to high and low topography, respectively). The anomalies of the SFGM, span between negative and positive values and their distribution, similar to those of the DFGM, is related to the masses excess and defect with respect to the 1D reference model. Another static forward modelling (named *SFGM_tc*), implemented by suppressing the effect of topography, enhances the effect of the density variations in the central subsided area, where strong positive anomalies are observed.
- The comparison between the *SFGM* with the observed gravity anomalies (gravity disturbance variations), shows that two fields are characterized by a similar alternation of weak positive and strong negative gravity anomalies. However, the modelled anomalies show a smoother trend and higher amplitude, being related to the density and topography variations induced by the upwelling of the asthenosphere, while the observed gravity field is strongly influenced by the sedimentation not simulated in our model. Knowledge of the stratigraphy of the *CB*, will allow including the effects of sedimentation/erosion on the basement depth variations in the future simulations, in order to increase the consistency of the results. In addition, starting from the results of this study, it will be possible to explore the effects of other tectonic processes on the *ICBs* evolution, such as the compressional stress related to the supercontinent assembly, implementing similar 3D numerical models.

- The deployment of more seismic stations in the African continent will offer the possibility to increase in the near future our knowledge on the crustal and mantle structures of an area that is still mostly uncovered of seismic data. As soon as this objective is achieved, it will be possible to increase the complexity of the 3D numerical models, by including more structural heterogeneities.

Uncited references

Allen and Armitage (2012), Amante and Eakins (2009), Burke and Gunnell (2008), Foley and O'Neil (2021), Kadima et al. (2011), Koptev et al., xxxx, Uieda et al. (2016), Tange (2021).

CRediT authorship contribution statement

Francesca Maddaloni : Investigation, Validation, Data curation, Writing – original draft, Visualization. **Magdala Tesauro :** Conceptualization, Validation, Investigation, Writing – original draft, Writing – review & editing, Visualization, Supervision, Project administration. **Taras V. Gerya :** Conceptualization, Methodology, Software, Writing – review & editing. **Alberto Pastorutti :** Methodology, Software, Investigation, Writing – review & editing. **Carla Braitenberg :** Conceptualization, Writing – review & editing, Supervision. **Damien Delvaux :** Writing – review & editing. **Jessica Munch :** Methodology, Software.

Declaration of Competing Interest

The authors declare that they have no known competing financial interests or personal relationships that could have appeared to influence the work reported in this paper.

Acknowledgements

A PhD grant to author Francesca Maddaloni was provided by Regione Friuli Venezia Giulia (Italy) through a European Social Fund (FSE) 50 % cofounded fellowship. Magdala Tesauro acknowledges the grant "INTRAcratonic basins TECTOnic evolution: The Congo Basin (INTRA-TECTO). The authors gratefully acknowledge the computational resources of the Dept. of Mathematics and Geosciences, University of Trieste, which were employed in the gravity forward modelling. GNU Parallel (Tange, 2021) was used to efficiently compute the gravity effect of a large number of prisms. Comments and suggestions of S. Cloetingh and L. Le Pourhiet significantly improved the original manuscript.

Appendix A. Supplementary material

Supplementary data to this article can be found online at https://doi.org/10.1016/j.gr.2022.09.002.

References

Allen, P.A., Armitage, J.J., 2012. Cratonic basins. In: Busby, C., Azor, A. (Eds.), Tectonics of Sedimentary Basins: Recent Advances. Blackwell Publishing Ltd., pp. 602–620. https://doi.org/10.1002/9781444347166.ch30.

Amante, C., Eakins, B.W., 2009. ETOPO1 1 arc-minute global relief model: procedures. data sources and analysis. NOAA Technical Memorandum NESDIS NGDC-24 19, pp.

Begg, G.C., Griffin, W.L., Natapov, L.M., O'Reilly, S.Y., Grand, S.P., O'Neill, C.J., Hronsky, J.M.A., Poudjom Djomani, Y., Deen, T., Bowden, P., 2009. The lithospheric architecture of Africa. Seismic tomography, mantle petrology and tectonic evolution. Geosphere 5, 23–50.

Boniface, N., Schenk, V., 2012. Neoproterozoic eclogites in the Paleoproterozoic Ubendian Belt of Tanzania: evidence for a Pan-African suture between the Bangweulu Block and the Tanzania Craton. Precambr. Res. 208–211, 72–89.

Buiter, S.J.H., Steinberger, B., Medvedev, S., Tetreault, J.L., 2012. Could the mantle have caused subsidence of the Congo Basin? Tectonophysics 514–517, 62–80. https://doi.org/10.1016/j.tecto.2011.09.024.

Burke, K., Gunnell, Y., 2008. The African erosion surface: a continental-scale synthesis geomorphology, tectonics, and environmental change over the past 180 million years. Geol. Soc. Am. Memoir 201, 66 pp.

Burov, E., Cloetingh, S., 2010. Plume-like upper mantle instabilities drive subduction initiation. Geophys. Res. Lett. 37, L03309.

Cacace, M., Scheck-Wenderoth, M., 2016. Why intracontinental basins subside longer: 3-D feedback effects of lithospheric cooling and sedimentation on the flexural strength of the lithosphere. J. Geophys. Res. Solid Earth 121, 3742–3761. https://doi.org/10.1002/2015JB012682.

Celli, N.L., Lebedev, S., Schaeffer, A.J., Gaina, C., 2020. African cratonic lithosphere carved by mantle plumes. Nat. Commun. 11, 92. https://doi.org/10.1038/s41467-019-13871-2.

Cloetingh, S., Koptev, A., Kovacs, I., Gerya, T., Beniest, A., Willingshofer, E., Ehlers, T.A., Andric-Tomasevic, N., Botsyun, S., Eizenhofer, P.R., Francois, T., Beekman, F., 2021. Plume-induced sinking of intracontinental lithospheric mantle: an overlooked mechanism of subduction initiation? Geochemistry Geophysics Geosystems, 22, e2020GC009482.

Crameri, F., Schmeling, H., Golabek, G.J., Duretz, T., Orendt, R., Buiter, S.J.H., May, D.A., Kaus, B.J.P., Gerya, T.V., Tackley, P.J., 2012. A comparison of numerical surface topography calculations in geodynamic modelling: an evaluation of the 'sticky air' method. Geophys. J. Int. 189, 38–54.

Crosby, A.G., Fishwick, S., White, N., 2010. Structure and evolution of the intracratonic Congo Basin. Geochem. Geophys. Geosyst. 11 (6), Q06010. https://doi.org/10.1029/2009GC003014.

Daly, M.C., Lawrence, S.R., Diemu-Tshiband, K., Matouana, B., 1992. Tectonic evolution of the Cuvette Centrale, Zaire. J. Geol. Soc. London 149, 539–546. https://doi.org/10.1144/gsjgs.149.4.0539.

De Wit, M.J., Linol, B., 2015. Precambrian basement of the Congo Basin and its flanking terrains. In: de Wit, M., Guillocheau, F., de Wit, M.C.J. (Eds.), the Geology and Resource Potential of the Congo Basin. Springer, Berlin, pp. 19–40. https://doi.org/10.1007/978-3-642-29482-2_2.

Delvaux, D., Maddaloni, F., Tesauro, M., Braitenberg, C., 2021. The Congo Basin: Stratigraphy and subsurface structure defined by regional seismic reflection, refraction and well data. Global Planet. Change 198, 103407. https://doi.org/10.1016/j.gloplacha.2020.103407.

Downey, N.J., Gurnis, M., 2009. Instantaneous dynamics of the cratonic Congo Basin. J. Geophys. Res. 114, B06401. https://doi.org/10.1029/2008JB006066.

Emry, E.L., Shen, Y., Nyblade, A.A., Flinders, A., Bao, X., 2019. Upper mantle earth structure in Africa from full-wave ambient noise tomography. Geochem. Geophys. Geosyst. 20, 120–147. https://doi.org/10.1029/2018GC007804.

Fernandez-Alonso, M., Cutten, H., De Waele, B., Tack, L., Tahon, A., Baudet, D., Barritt, S.D., 2012. The Mesoproterozoic Karagwe-Ankole Belt (formerly the NE Kibara Belt): The result of prolonged extensional intracratonic basin development punctuated by two short-lived far-field compressional events. Precambr. Res. 216–219, 63–86.

Finger, N.-P., Kaban, M. K., Tesauro, C., Mooney, W. D., Thomas, M., 2022. A Thermo-Compositional Model of the African Cratonic Lithosphere. Geochemistry, Geophysics, Geosystems (accepted).

Fishwick, S., 2010. Surface wave tomography: Imaging of the lithosphere–asthenosphere boundary beneath central and southern Africa. Lithos 63–73. https://doi.org/10.1016/j.lithos.2010.05.011.

Foley, S., O'Neil, C., 2021. Continents soldered from below. Nature 592, 692.

Gerya, T.V., 2019. Introduction to numerical geodynamic modelling, Second edition. Cambridge University Press, Book.

Gerya, T.V., Burov, E.T., 2018. Nucleation and evolution of ridge-ridge-ridge triple junctions: thermomechanical model and geometrical theory. Tectonophysics 746, 83–105. https://doi.org/10.1016/j.tecto.2017.10.020.

Gerya, T.V., Stern, R.J., Baes, M., Sobolev, S.V., Whattam, S.A., 2015. Plate tectonics on the Earth triggered by plume-induced subduction initiation. Nature 527, 221–225. https://doi.org/10.1038/nature15752.

Gerya, T.V., Yuen, D.A., 2007. Robust characteristics method for modelling multiphase visco-elasto-plastic thermo-mechanical problems. Phys. Earth Planet. Inter. 163, 83–105.

Goldberg, A.S., 2010. Dyke swarms as indicators of major extensional events in the 1.9–1.2 Ga Columbia supercontinent. J. Geodyn. 50, 176–190. https://doi.org/10.1016/j.jog.2010.01.017.

Gurnis, M., 1988. Large-scale mantle convection and the aggregation and dispersal of supercontinents. Nature 332, 695–699.

Heine, C., Müller, R.D., Steinberger, B., Torvisk, T.H., 2008. Subsidence in intracontinental basins due to dynamic topography. In: Physics of the Earth and Planetary Interiors. https://doi.org/10.1016/j.pepi.2008.05.008.

Hu, J., Faccenda, M., Zhou, Q., Fischer, K.M., Marshak, S., Lundstrom, C., 2018. Modification of the Western Gondwana craton by plume lithosphere interaction. Nat. Geosci. 11, 203–210.

Kadima, E.K., Sebagenzi, S.M.N., Lucazeau, F., 2011. A Proterozoic-rift origin for the structure and the evolution of the cratonic Congo Basin. Earth Planet. Sci. Lett. 304, 240–250.

Klein, G., Hsui, A.T., 1987. Origin of cratonic basins. Geology 15, 1094–1098.

Koptev, A., Calais, E., Burov, E., Leroy, S., Gerya, T., 2015. Dual continental rift systems generated by plume–lithosphere interaction. Nat. Geosci. 8, 388–392. https://doi.org/10.1038/NGEO2401.

Koptev, A., Cloetingh, S., Kovács, I.J., Gerya, T., Ehlers, T.A., Controls by rheological structure of the lithosphere on the temporal evolution of continental magmatism: Inferences from the Pannonian Basin system. Earth Planet. Sci. Lett. 565, 116925.

Koptev, A., Gerya, T., Calais, E., Leroy, S., Burov, E., 2018. Afar triple junction triggered by plume-assisted bi-directional continental break-up. Sci. Rep. 8, 14742.

Korsch, R.J., Lindsay, J.F., 1989. Relationships between deformation and basin evolution in the Amadeus basin, Central Australia. Tectonophysics 158, 5–22.

Lindsay, J.F., 2002. Supersequences, superbasins, supercontinents-evidence from the

Neoproterozoic-Early Paleozoic basins of Central Australia. Basin Res. 14, 207–223.
Linol, B., de Wit, M.J., Guillocheau, F., Robin, C., Dauteuil, O., 2015. Multiphase Phanerozoic subsidence and uplift history recorded in the Congo Basin: a Complex successor basin. In: de Wit, M., Guillocheau, F., de Wit, M.C.J. (Eds.), the Geology and Resource Potential of the Congo Basin. Springer, Berlin, pp. 213–227. https://doi.org/10.1007/978-3-642-29482-2_11.
Liu, J., Graham Pearson, D., Wang, L.H., Mather, K.A., Kjarsgaard, B.A., Schaeffer, A.J., Inrvine, G.J., Kopylova, M.G., Armstrong, J.P., 2021. Plume-driven recratonization of deep continental lithospheric mantle. Nature 592. https://doi.org/10.1038/s41586-021-03395-5.
Lucazeau, F., Armitage, J., Kadima, E.K., 2015. Thermal regime and evolution of the Congo Basin as an intracratonic basin. In: de Wit, M., Guillocheau, F., de Wit, M.C.J. (Eds.), the Geology and Resource Potential of the Congo Basin. Springer, Berlin, pp. 229–1224. https://doi.org/10.1007/978-3-642-29482-2_12.
Maddaloni, F., Braitenberg, C., Kaban, M.K., Tesauro, M., Delvaux, D., 2021. The Congo Basin: Subsurface structure interpreted using potential field data and constrained by seismic data. Global Planet. Change 205, 103611. https://doi.org/10.1016/j.gloplacha.2021.103611.
Munch, J., Gerya, T., Ueda, K., 2020. Oceanic crust recycling controlled by weakening at slab edges. Nat. Commun. 11, 2009.
Nance, R.D., Murphy, J.B., Santosh, M., 2013. The supercontinent cycle: a retrospective essay. Gondwana Res. 25, 4–29. https://doi.org/10.1016/j.gr.2012.12.026.
Ojo, A.O., Weisen, S., Ni, S., Zhao, L., Xie, J., Kao, H., 2022. Lithospheric structure of Africa and surrounding regions revealed by earthquake and ambient noise surface wave tomography. J. Geophys. Res. (under review). https://doi.org/10.1002/essoar.10504718.1.
Pasyanos, M.E., Nyblade, A.A., 2007. A top to bottom lithospheric study of Africa and Arabia. Tectonophysics 444, 27–44. https://doi.org/10.1016/j.tecto.2007.07.008.
Perron, P., Guiraud, M., Vennin, E., Moretti, I., Portier, É. Le Pourhiet, L. and Konaté, M., 2018. Influence of basement heterogeneity on the architecture of low subsidence rate Paleozoic intracratonic basins (Reggane, Ahnet, Mouydir and Illizi basins, Hoggar Massif), Solid Earth, 9(6), 1239-1275, Doi: 10.5194/se-9-1239-2018, 2018.
Perron, P., Le Pourhiet, L., Guiraud, M., Vennin, E., Moretti, I., Portier, É., Konaté, M., 2020. Control of inherited accreted lithospheric heterogeneity on the architecture and the low long-lived subsidence rate of intracratonic basins. BSGF - Earth Sci. Bull. 200024, 2020. https://doi.org/10.1051/bsgf/2020038.
Phillips, B.R., Bunge, H.-P., 2007. Supercontinent cycles disrupted by strong mantle plumes. Geology 35, 846–850.
Poudjom, Y.H.D., O'Reilly, S.Y., Griffin, W.L., Morgan, P., 2001. The density structure of subcontinental lithosphere through time. Earth Planet. Sci. Lett. 184, 605–621.
Ranalli, G., 1995. Rheology of the Earth. Chapman & Hall, London.
Sebai, A., Stutzmann, E., Montagner, J.P., Sicilia, D., Beucler, E., 2006. Anisotropic structure of the African upper mantle from Rayleigh and Love wave tomography. Phys. Earth Planet. Inter. 155 (1–2), 48–62.
Tange, O., 2021. GNU Parallel. Zenodo. https://doi.org/10.5281/zenodo.5013933.
Uieda, L., Barbosa, V., Braitenberg, C., 2016. Tesseroids: Forward-modeling gravitational fields in spherical coordinates. Geophysics F41–F48. https://doi.org/10.1190/geo2015-0204.1.